

1 Multi-Scale Equatorial Electrojet Turbulence

2 I. Baseline 2D Model

Ehab Hassan,^{1,3} W. Horton,^{1,2} A.I. Smolyakov^{4,5} D.R. Hatch^{1,6} S.K. Litt,⁴

¹Department of Physics, University of
Texas at Austin, Austin, Texas, USA.

²Applied Research Laboratory, University
of Texas at Austin, Austin, Texas, USA.

³Department of Physics, Ain Shams
University, Cairo, Egypt.

⁴Department of Physics and Engineering
Physics, University of Saskatchewan,
Saskatoon, Canada

⁵International Institute of Fusion Science,
University of Aix-Marseille, Marseille,
France

⁶Institute for Fusion Studies, University
of Texas at Austin, Austin, Texas, USA.

Abstract. The spatial and spectral characteristics of the turbulent plasma density, electric fields, and ion drift in ionospheric E-region are studied using a new set of nonlinear plasma fluid equations. The fluid model combines both Farley-Buneman (Type-I) and Gradient-Drift (Type-II) plasma instabilities in the equatorial electrojet. In our unified model of the plasma instabilities we include the ion viscosity in the ion momentum equation and electron inertia in the electron momentum equation. These two terms play an important role in stabilizing the growing modes in the linear regime and in driving the Farley-Buneman instability into the saturation state. The simulation results show good agreements with a number of features of rocket and radar observations, such as: (1) saturation of plasma density perturbations depends on the solar condition and reaches 7-15% relative to the background, (2) fluctuation of the horizontal secondary electric field reaches 8-15 (mV/m), (3) stabilization of the phase velocity of the perturbed density wave around the value of the ion-acoustic speed inside the electrojet, (5) "up-down" asymmetry in the vertical fluxes of the plasma density, (6) "east-west" asymmetry of the plasma zonal drifts, and (7) generation of small-scale of the order of meter scale lengths irregularities embedded in large-scale structures. Spectral analysis of the density fluctuations reveals the energy cascade due to the nonlinear coupling between structures of different scales. The break-up of the large-scale structures into small-scale structures explains the disappearance of Type-II echoes in the presence of Type-I instabilities.

1. Introduction

The Earth's ionosphere is rich with plasma irregularities of various scale-lengths extending from a few centimeters to hundreds of kilometers [Farley and Balsley 1973, Fejer 1980]. At times during which the ionosphere is disturbed, mixed plasma states occur with large-scale coherent structures such as plumes, bubbles and vortices along with high levels of meter-scale incoherent plasma turbulence. These dynamics are important from both fundamental and applied perspectives. The combination of small-scale turbulence with large-scale coherent structures is at the forefront of basic plasma turbulence theory, while the spatial and spectral characteristics of the evolution of the electron density in the E-region is important for terrestrial navigation and communication systems [Wernik 2003] which resolution is often limited by the turbulence in ionospheric plasma density.

In the equatorial E-region of Earth's ionosphere, the Farley-Buneman instability is driven by an intense equatorial eastward electrojet current [Richmond 1973, Rishbeth 1997]. The Farley-Buneman instability is identified in the backscattering radar data as Type-I turbulent echoes, e.g. as observed by the coherent backscattering radar at Jicamarca [Bowles *et al.* 1963, Fejer 1975, Hysell 2007] and theoretically studied by Farley [1963] and Buneman [1963].

The electrons are magnetized ($\nu_{en} \ll \omega_{ce}$) and experience $-\mathbf{U} \times \mathbf{B}$ drifts in the E-region, while the ions are unmagnetized ($\nu_{in} \gg \omega_{ci}$) so they are tied to the neutral gas and experience \mathbf{U} drifts, where \mathbf{U} is the speed of the neutral wind. The E-region, extending between altitudes 90-120 km, is found to be the most conductive region in the ionosphere owing to the large Cowling conductivity, $\sigma_C = \sigma_P(1 + \sigma_H^2/\sigma_P^2)$, which depends on the ra-

46 tio between the Hall, σ_H , and the Pedersen, σ_P , conductivities [Baker and Martyn 1953].
 47 This large Hall-to-Pedersen conductivity ratio, which reaches its maximum value of 15-
 48 20 between 104-105 km, allows the electron drift velocity, v_E , to exceed the ion-acoustic
 49 speed $C_s = \sqrt{(T_e + \gamma_i T_i)/m_i}$ by a factor that is large enough to drive the Farley-Buneman
 50 instability.

51 In addition to the Farley-Buneman instability, density gradients can also drive another
 52 type of instability in the ionosphere. The gradient-drift instability is identified in the
 53 backscattering radar data as Type-II turbulent echoes, e.g. as observed by the coher-
 54 ent backscattering radar at Jicamarca [Bowles *et al.* 1963, Fejer 1975, Hysell 2007].
 55 The density gradient drive instability mechanism was studied by Simon [1963] and Hoh
 56 [1963]. From the bottom of the E-region to the peak of the F-region, the ionosphere
 57 is subject to strong drift wave type plasma turbulence owing to the upward increase of
 58 the electron density. The electron density between 90-110 km has an exponential profile
 59 $n(z) = n_o \exp(z/L_n)$ perpendicular to the flowing current, \hat{y} , and the geomagnetic field \hat{x} ,
 60 where \hat{z} is the unit vector in the vertical upward direction and $L_n^{-1} = \partial_z \ln n$ is the electron
 61 density vertical gradient length scale. The gradient-drift instability can be excited by little
 62 or no threshold drift speed, which makes it more easy to excite than the Farley-Buneman
 63 instability. Farely and Balsley [1973] used the linear theory to get a relation between
 64 the threshold drift speed of the gradient-drift waves and their wavelength and have to
 65 be $v_E > k^2 C_s^2 \left[\frac{1 + \nu_{en} \nu_{in} / \omega_{ce} \omega_{ci}}{\nu_{in} \omega_{ce} / \nu_{en}} \right] L_n$. Hence, we can have gradient-drift waves with a broad
 66 range of wavelengths; as long as kilometers and as small as tens of meters. However, it is
 67 not possible to find linearly growing gradient-drift waves of the order of meters because
 68 they require drift speeds much higher than what is measured and found in the equatorial

electrojet region.

During the nighttime the recombination process happens very fast and we have regions of positive and negative gradient-drifts distributed randomly around the globe [Kudeki *et al.* 1982]. The gradient-drift instability is driven by the $\mathbf{E} \times \mathbf{B}$ drift instability due to gradients in electron density and dominates at small wavenumbers.

Both Type-I and Type-II have been extensively studied in the past by many authors. In contrast, in this work, we introduce a unified model describing both the Type-I and Type-II modes in the ionospheric E-region. The dominant nonlinear coupling mechanism is the $\mathbf{E} \times \mathbf{B}$ convection of the fluctuating density described mathematically by a Poisson bracket or a Jacobian nonlinearity [Horton and Hasegawa 1994, Horton and Ichikawa 1997].

This paper is organized as follows. In next section we review the rocket measurements and radar observations and related theoretical work. In section(3) we present the physical model that describes the nonlinear dynamics of both Farley-Buneman and gradient-drift instabilities. The linear limit of this dynamical system and linear results are discussed in section(4). The nonlinear simulations and results are presented in section(5). We end the paper with a summary of all results and the conclusions we can draw from these results to explain the observations.

2. Observations and Theoretical Models

2.1. Observations

Bowles *et al.* [1963] used the radar backscattering experiment at 50 MHz at Jicamarca, Peru to study the echoes of the field-aligned irregularities in the equatorial electrojet

(EEJ). Later, the experiment was repeated for different case studies by Cohen *et al.* [1967], Balsley [1969], Balsley and Farley [1971, 1973], Farley and Balsley [1973], and Fejer *et al.* [1975, 1976] in order to examine the characteristics of the backscattered echoes with the goal of understanding the mechanisms of the E-region plasma irregularities at the equator and high-latitudes.

When the electron drift velocity in the equatorial electrojet exceeds the ion-acoustic speed, an echo spectrum appears simultaneously at all elevations and its Doppler shift always equals the ion-acoustic speed to a good approximation. The spectrum of the echoes is characterized by a spectral width narrower than the echoes' Doppler shift. The Doppler shift of the echoes is isotropic in the angle between the horizontal plane and the wave propagation wavevector, θ . The instability with these characteristics is called Type-I instability [Bowles *et al.* 1963, Balsley 1969, Fejer *et al.* 1975].

However, as the electron drift speed falls below the ion acoustic speed, the backscattered radar echoes exhibit different spectral characteristics and we have now what is called Type-II instability. Despite the increase of the spectral width of Type-II echoes with the wavenumber, it does not change with the elevation angle. The Doppler shift of Type-II instability varies as the cosine of the angle between the horizontal plane and the wave propagation wavevector, θ , and varies linearly with the wavenumber at constant angle θ [Bowles *et al.* 1963, Balsley 1969, Fejer *et al.* 1975, Hanuise and Chrochet 1981]. Type-II instability is always easily excited in the presence of a density-gradient [Simon 1963, Hoh 1963, Maeda *et al.* 1963, Knox 1964, Reid 1968, Rogister and D'Angelo 1970, Balsley and Farely 1971] and owing to the absence of a real electron drift threshold [Farely and Balsley 1973], type-II instability is difficult to observe in the presence of type-I instability

which is excited in a strong turbulence mechanism [Sudan *et al.* 1983].

The echoes for Type-I and Type-II instabilities can be seen both during the daytime and nighttime. The strong damping of the instabilities above 115 km, as a result of the carrier's recombinations processes and the negative density scale-length, limits these echoes in the daytime to the region between 93 and 113 km. However, the irregularity in the electron density profile during the nighttime, which gives rise to irregularity in the density gradient, extends the instabilities beyond 113 km and the echoes can be seen up to 130 km [Kudeki 1987]. Shortly after sunset the radar backscattered data of the electrojet shows an inverse of the sign of its phase velocity. The change of the sign of the phase velocity is considered an evidence of the reversal of the equatorial electrojet, where the electrons reverse the daytime westward flow to an eastward flow during the nighttime. This electrojet reversal is accompanied by a disappearance of the instabilities echoes [Fejer *et al.* 1975].

Farley and Balsley [1971] shows the radar data at 50 MHz and 146-MHz frequencies that emphasize the dominance of the Type-I instability in the spectrum of the radar echoes at both frequencies when the electrons drift reaches the threshold of Type-I instability as it is exceeding the ion-acoustic speed ($v_E \geq C_s$). There is no, however, practical threshold for Type-II instability, as we discussed earlier, that can be detected at the HF radar echoes (50-MHz) but type-II echoes can not be seen at the VHF radar echoes (150-MHz).

These measurements indicate the presence of irregularities of different scale lengths that range from a kilometer or tens of meters scales due to pure type-II instability down to a meter or shorter due to pure type-I instability.

Pfaff *et al.* [1987] showed the data collected from sounding rocket launched from Punta,

Lobos, Peru in order to quantify the plasma instabilities by detecting the turbulence in the daytime plasma density and electrostatic field in the equatorial electrojet. A simultaneous measurement taken by the Jicamarca radar showed strong type-I echoes of 3 m wavelength accompanied with long-scale horizontally propagating waves. The data showed instability in the plasma density in the region of the positive vertical gradient between 90-110 km altitude with maximum variations of spectral energy measured at frequencies below 100 Hz.

Later, Pfaff *et al.* [1997] described the measurements gathered from the in-situ sounding rocket that was launched from *Alântara*, Brazil in 1994. Pfaff found a maximum daytime vertical electric field of about 9-10 mV/m near 105 km altitude coincident with a maximum current density of magnitude $8.0\mu A/m^2$. The maximum vertical electric field corresponds to 360-400 m/s westward electron drift, which is about the ion-acoustic speed calculated at the same altitude. These measurements agree with the estimated large electrojet Hall current and Cowling conductivity estimated at about the same altitude.

Recently, a combined system of five radars was used at Jicamarca on July 26, 2006 to monitor the equatorial electrojet, including range-time-intensity (RTI) mapping, radar imaging, radar oblique scattering, Faraday rotation, and multiple frequency scattering using AMISR prototype UHF radar [Hysell *et al.* 2007]. Radar imaging data shows narrow type-I echoes excited from the vertically polarized electric field of the large-scale waves which is different from the type-I echoes excited directly by the background electrojet current. Hysell *et al.* [2007] found stronger echoes come from the upward flux at the spectrograms from the AMISR prototype at Jicamarca and considered that as an evidence of "updown" asymmetry in the vertical particle fluxes. In addition, an asymmetry in the

irregularity drifts is found in "east-west" direction with more westward drift during the daytime.

2.2. Theoretical Interpretations

Sudan *et al.* [1973] uses the two-step mechanism to explain the generation of the meter scale Type-II irregularities detected by 50-MHz incoherent scattering radar at electron drifts of order 100 m/s. The gradient-drift instability is excited in the daytime with positive gradient and westward drift of the electron. When the amplitude of large-scale instability reaches a certain level, the energy starts to transfer from that primary long-wavelength waves to secondary short-wavelength waves. This energy transfer takes place due to the strong perturbations of the electrojet local parameters, where the horizontal density gradient becomes greater than the background vertical gradients and the magnitude of the vertically perturbed drifts increases to the order of magnitude of the horizontal electron drift [Farely and Balsley 1973]. However, the excitation of vertical irregularities of wavelength of the order of meters or sub-meter is a pure type-I nonlinear mechanism that takes place only when the electron drifts exceed the ion-acoustic speed [Sudan *et al.* 1973].

On the other hand, the dependence of the phase velocity of type-I instability on the cosine of the angle between the horizontal plane and the wave propagation wavevector, θ , in the linear theory is not supported by the observations [Sudan 1983a]. The phase velocity which equals the Doppler shift is independent of the angle θ and has a constant value that equals the ion-acoustic speed [Balsley 1969, Farely and Balsley 1973, Hanuise and Crochet 1981]. Kamanetskaya [1971] and Rogister [1971], Kaw [1972], Skadron and Weinstock [1969], Weinstock and Sleeper [1972], Rogister and Jamin [1975], and Jamin

and Kennel [1976] suggested various mechanism to explain these observations such as the quasilinear theory that limits v_E to C_s , the refraction of waves in the electrojet velocity profile, the nonlinear orbital diffusion of ions or electrons, mode coupling outside the instability cone, and the propagation with finite k_{\parallel} along the magnetic field, respectively, but they all rely on incorrect hypotheses by either treating type-I and type-II instabilities independently [Sudan 1983a] or considering homogeneous electrojet [Farely and Balsley 1973].

Sudan [1983a, 1983b] has also treated this problem differently by considering the co-existence of the two types of instabilities and the effect of the developed type-II strong turbulence on the evolution and development of type-I instability. Sudan [1983b] suggested that the nonlinear process modifies the electron-neutral collision frequency ν_{en} by wave-amplitude dependent value that causes the growth rate to vanish in the saturation region.

3. Plasma Dynamics and Model Equations

The E-region is bounded by two layers of reduced conductivities; below 90 km the collision frequencies of the charge carriers with background neutrals are very high, reducing the conductivity to very small values, whereas above 130 km both the electrons and the ions are magnetized and are influenced by the Lorentz force which also reduces the conductivity to very small value. According to the sounding rocket data, the maximum conductivity is centered at 105 km. Hence, any vertical current will be inhibited by a vertically induced electric field as a result of the accumulation of the electrons at the upper layer and the accumulation of the heavy ions at the lower layer. We adopt a slab geometry model with the x-axis pointing northward along the geomagnetic field which is

perpendicular to the plane in which the dynamical equations are written, y-axis pointing westward, and the z-axis pointing vertically upward, as shown in figure(1).

The possible nonlinear coupling mechanisms between the linear unstable modes is shown in figure(1-a,b). The forward-cascade coupling mechanism in figure(1-a) shows the interaction between nearly collinear modes to produce a mode of shorter wavelength. However, the interaction between two unstable modes of short wavelength to produce a stable mode of longer wavelength in an inverse-cascade coupling mechanism is shown in figure(1-b). Kudeki and Farley [1989] and Lu *et al.* discussed the sensitivity of the aspect angel of the equatorial electrojet irregularities and the coupling mechanism between the linearly unstable modes.

3.1. Dynamic System Equations

In our model, we have three dynamical equations for three fields; the plasma density n , the electric potential φ , and the ion velocity potential χ . The ion density profile of all species shows that O_2^+ is the dominant ion species in the E-region, and we consider only one ion species. We assume isothermal state, $T_e = T_i$, and quasineutrality, $n_e = n_i$, since the electron Debye length, $\lambda_D \approx 1cm$, is much smaller than the spatial variation of the electron density. The small ratio between the ion gyrofrequency, ω_{ci} , and the ion-neutral collision frequency, ν_{in} , makes the mean-free path of the ions small so that ions cannot complete one gyrocycle before experiencing another collision. Therefore, the ions are considered unmagnetized and we ignore the Lorentz force, $v_i \times \mathbf{B}$; in the ion's equation of motion. However, the electrons are considered magnetized since the ratio between the electron gyrofrequency, ω_{ce} , and the electron-neutral collision frequency, ν_{in} , is much larger than unity [Kelley 2009]. Finally, the acceleration due to gravity in both equations

of motion is ignored.

The negligible variations of the equatorial geomagnetic field, $\delta B_o = 20nT$, with respect to the background geomagnetic field, $B_o = 30\mu T$, makes us consider an electrostatic plasma with the electric field is defined as $\mathbf{E} = -\nabla\varphi$. Also, the ion fluid velocity can be written as $\mathbf{v}_i = -\nabla\chi$.

The ion's continuity equation and the equations of motion of electrons and ions can be written in their general forms as:

$$\partial_t n + \nabla \cdot (n\mathbf{v}_i) = 0 \quad (1)$$

$$m_i n \Delta_t \mathbf{v}_i = en\mathbf{E} - T_i \nabla n - \nabla \cdot \bar{\bar{\pi}} - m_i n \nu_{in} \mathbf{v}_i \quad (2)$$

$$m_e n \Delta_t \mathbf{v}_e = -en(\mathbf{E} + \mathbf{v}_e \times \mathbf{B}) - T_e \nabla n - m_e n \nu_{en} \mathbf{v}_e \quad (3)$$

where, Δ_t is the convective derivative; $\Delta_t \equiv (\partial_t + \mathbf{v} \cdot \nabla)$, and $\bar{\bar{\pi}}$ is the ion viscosity stress tensor and its elements are given by:

$$\pi_{\alpha\beta} = -\frac{nT_i}{\nu_{in}} \left(\partial_\beta v_\alpha + \partial_\alpha v_\beta - \frac{2}{3} \nabla \cdot \mathbf{v} \delta_{\alpha\beta} \right) \quad (4)$$

In this model we consider the ion viscosity and the electron inertia. The physics of these two terms and their effects on the stabilization of the growth rate and the saturation of the instabilities will be explained later.

Equations (1) and (2) can be rewritten in terms of the normalized quantities ($\tilde{n} = n/n_o$, $\tilde{\varphi} = e\varphi/T_e$, and $\tilde{\chi} = \chi/1$) as:

$$\partial_t \tilde{n} = \nabla \tilde{n} \cdot \nabla \tilde{\chi} + \tilde{n} \nabla^2 \tilde{\chi} \quad (5)$$

$$\partial_t \nabla^2 \tilde{\chi} = \nabla^2 \left(v_{ti}^2 \tilde{n} + v_{ti}^2 \tilde{\varphi} - \nu_{in} \tilde{\chi} + (\nabla \tilde{\chi})^2 \right) + \frac{4}{3} \frac{v_{ti}^2}{\nu_{in}} \nabla^4 \tilde{\chi} \quad (6)$$

The magnetized electron drift velocity, in a plane perpendicular to the geomagnetic field, can be given after some algebraic manipulation of equation(3) as

$$\mathbf{v}_{e\perp} = \frac{e}{m_e \Omega_{ce}} \left[\hat{\mathbf{b}} \times + \frac{\nu_{en}}{\Omega_{ce}} + \frac{\Delta_t}{\Omega_{ce}} \right] \nabla \left[\varphi - \frac{T_e}{e} \ell n n \right],$$

and for the first-order approximation we can rewrite the electron velocity as

$$\mathbf{v}_{e\perp} = \mathbf{v}_E + \mathbf{v}_{de} + \mathbf{v}_{Pe} + \mathbf{v}_\nu \quad (7)$$

where, \mathbf{v}_E is the $\mathbf{E} \times \mathbf{B}$ drift velocity, \mathbf{v}_{de} is the diamagnetic drift velocity, \mathbf{v}_{Pe} is the polarization drift velocity, and \mathbf{v}_ν is the drift velocity due to the frictional force between the electrons and the neutral background.

Substituting the ion drift velocity, $\mathbf{v}_i = -\nabla \chi$, and the electrons drift velocity from equations (7) in the plasma quasineutrality condition, $\nabla \cdot (\mathbf{J}_i + \mathbf{J}_e) = 0$, and by making some algebraic manipulation along with using the normalized quantities mentioned above, we can close our system with the following normalized dynamic equation:

$$\begin{aligned} \partial_t \nabla^2 \tilde{\varphi} &= \nu_{en} \nabla \tilde{n} \cdot \nabla \tilde{n} - \nu_{en} \nabla \tilde{n} \cdot \nabla \tilde{\varphi} + \rho_e^{-2} \nabla \tilde{n} \cdot \nabla \tilde{\chi} \\ &+ \nu_{en} \nabla^2 \tilde{n} - \nu_{en} \nabla^2 \tilde{\varphi} - \rho_e^{-2} \nabla^2 \tilde{\chi} \\ &- \Omega_{ce} [\tilde{\varphi}, \tilde{n}] - \rho_e^2 \Omega_{ce} [\tilde{\varphi}, \nabla^2 \tilde{\varphi}] \end{aligned} \quad (8)$$

where, $[f, g]$ is the Poisson (*Jacobian*) bracket which is defined as $[f, g] = \partial_x f \partial_y g - \partial_x g \partial_y f$.

3.2. Instabilities Evolution and Saturation

The ion viscosity term in equation(6), $\frac{4}{3} \frac{v_{ti}^2}{\nu_{in}} \nabla^4 \tilde{\chi}$, plays an important role in stabilizing the modes at the large k-values and it simulates the effect of Landau damping, which can not represented in the fluid models. The effect of this term on the growth-rate is discussed in more detail in section(4).

In equation(8), the Jacobian $-\Omega_{ce} [\delta\tilde{\varphi}, \delta\tilde{n}]$ has a coefficient that is two- and four-orders of magnitude larger than the coefficients of the other terms, and it shows the coupling between the horizontal and the vertical waves in the electrojet. In addition, this Jacobian bracket is responsible for the generation of the vertical structures with the downward/upward drifts of the low/high density plasma which is driven by the gradient-drift instability.

On the other hand, the Jacobian bracket $-\rho_e^2 \Omega_{ce} [\delta\tilde{\varphi}, \nabla^2 \delta\tilde{\varphi}]$, which considers the $\mathbf{E} \times \mathbf{B}$ drift of the plasma vortices, adds more damping to the growing modes at high k-values to drive the system to saturation when the electron density amplitude grows linearly to (12%-25%) of its initial value at the beginning of the simulation, depending on the solar conditions.

Hence, the dynamics of the electron density, electric potential, and the ion velocity potential of the ionosphere plasma at a plane perpendicular to the geomagnetic field in the equatorial E-region can be described by a set of hyperbolic partial differential equations (5), (6), and (8).

4. Linear Regime

First we study the basic properties of the instabilities in the linear regime.

4.1. Dynamic System Linearization

To study the linear characteristics of the dynamical system, n, φ, χ , we need to linearize the equations (5,6,8). The linearized quantities for density n , electric potential φ , and ions drifts potential χ , with the assumption of a stationary background plasma $\nabla\chi_o = 0$, are:

$$n = n_o + \delta n, \quad \varphi = \varphi_o + \delta \varphi, \quad \chi = \delta \chi$$

where the general spectral representation of the fluctuations of the perturbed part of those three fields in space and time is given by:

$$\delta \phi(i = 1, 2, 3) = \sum_{k_x, k_y} \phi_i \exp [i(\mathbf{k} \cdot \mathbf{x} - \omega t)]$$

with a condition for real values giving $\phi_n(-k, -\omega^*) = \phi_n^*(k, \omega)$. where $(\delta \phi_1, \delta \phi_2, \delta \phi_3)$ are equivalent to $(\delta n, \delta \varphi, \delta \chi)$, respectively.

After dropping the zero-order and higher order terms the set of linearized and normalized equations is:

$$\partial_t \delta \tilde{n} = \nabla^2 \delta \tilde{\chi} \quad (9)$$

$$\partial_t \nabla^2 \delta \tilde{\varphi} = \quad (10)$$

$$\begin{aligned} & \left(\nu_{en} \nabla^2 - \frac{v_E}{\rho_e^2} \partial_y + \frac{v_E \nu_{en}}{\rho_e^2 \omega_{ce}} \partial_z + \frac{2\nu_{en}}{L_n} \partial_z \right) \delta \tilde{n} \\ & - \left(\nu_{en} \nabla^2 + v_E \partial_y \nabla^2 + \frac{\Omega_{ce}}{L_n} \partial_y + \frac{\nu_{en}}{L_n} \partial_z \right) \delta \tilde{\varphi} \\ & - \left(\frac{1}{\rho_e^2} \nabla^2 + \frac{1}{\rho_e^2 L_n} \partial_z \right) \delta \tilde{\chi} \\ & \partial_t \delta \tilde{\chi} = v_{ti}^2 \delta \tilde{n} + v_{ti}^2 \delta \tilde{\varphi} - \left(\nu_{in} - \frac{4}{3} \frac{v_{ti}^2}{\nu_{in}} \nabla^2 \right) \delta \tilde{\chi} \end{aligned} \quad (11)$$

where $\rho_e = v_E / \omega_{ce}$ is the electron gyroradius, $L_n = \partial_z \ell n n_o$ is the electron density scale-length that has an approximate value of 6 km (1 km) during the daytime (nighttime) with n_o as the background average charge-carrier density, and $v_E = -B_o^{-1} \partial_z \varphi_o$ is the $\mathbf{E} \times \mathbf{B}$ drift speed (≈ 400.0 m/s) with φ_o as the background average electric potential.

The analytical solution of the set of three linearized equations of the dynamical system for the three normalized quantities gives rise to a cubic dispersion equation as shown in

equation(11):

$$\begin{aligned}
D(\omega, k_y, k_z) = & \omega^3 + i\omega^2 \left[\nu_{en} + \nu_{in} \left(1 + \frac{4}{3} k_{\perp}^2 \frac{v_{ti}^2}{\nu_{in}} \right) \right] \\
& - \omega \left[\nu_{en} \nu_{in} \left(1 + \frac{4}{3} k_{\perp}^2 \frac{v_{ti}^2}{\nu_{in}} \right) + \left(1 + k_{\perp}^2 \rho_e^2 \right) \frac{v_{ti}^2}{\rho_e^2} \right] \\
& - i k_{\perp}^2 v_{ti}^2 \left[2\nu_{en} + i \frac{k_y}{k_{\perp}^2} \left(\left(1 + k_{\perp}^2 \rho_e^2 \right) \frac{v_E}{\rho_e^2} - \frac{\Omega_{ce}}{L_n} \right) \right]
\end{aligned} \tag{12}$$

4.2. Numerical Solution of Linear System

The local and the nonlocal approximations have been used to model plasma instabilities in the E-region depending on the relation between the density scale-length, L_n and the fluctuation wavenumber, k [Ronchi 1989]. We use the local approximation, valid in the case of $|kL_n| \gg 1$ (or $L_n \gg \lambda$, where $k = 2\pi/\lambda$), which is the condition that is satisfied in this study for the length of the type-II irregularities smaller than a kilometer.

We employ the the International Reference Ionosphere (IRI2007), Naval Research Laboratory Mass Spectrometer and Incoherent Scatter Radar Exosphere (NRLMSIS00), and International Geomagnetic Reference Field (IGRF11) empirical models under different conditions to get the altitude-dependent values of the collision frequencies, gyrofrequencies, and gyroradii for ions and electrons, as shown in table(1) for the solar-maximum and solar-minimum conditions.

4.3. Altitude Dependent Growth Rate

To study the altitude-dependence of the instabilities in our unified model we solve numerically the eigenvalue problem of the set of linearized equations (9,10,11) between 90-120 km to find the growth rates and phase velocities at each altitude. We use 0.03 m^{-1} resolution in k-space and 0.25 km resolution along the altitude, z-axis.

The growth rate profile as a function of altitude is shown in figure(2) and divides the

E-region into three regions. The lower region below 103 km shows a dominance of the pure gradient-drift (type-II) instability over the small wavenumbers with the absence of Farelly-Buneman instability at the intermediate and large wavenumbers due to the large collision rates of plasma species with the ionosphere neutral background and the small relative speed between the electrons and ions. The region extends between 110-115 km does not have instabilities at small wavenumbers which reflects the absence of gradient-drift instability as a result of the negative scale-length of the plasma density. The growing modes in this region are found in the intermediate and large wavenumbers where the pure Farelly-Buneman (type-I) instability dominates. A coupling between type-I and type-II instabilities can be seen at the core of the electrojet region between 103-110 km, where the maximum positive growth rate extends over all wavelength scales from hundreds or tens of meters to sub-meter.

Thus, the altitude-dependent growth rate profile is in agreement with the rocket observations that divides the instabilities in the equatorial electrojet region into three regions as we described with the peak of the electrojet turbulence between 103-108 km [Pffaf 1987b].

4.4. Standard Model versus Unified Model

In figure(3) we demonstrate the effect of the ion viscosity term, $\nabla^4\chi$, and the electron inertia term, $\partial_y\nabla^2\varphi$, which both are stabilizing at high wavenumbers for a reference case at 105 km altitude. When the electron inertia is ignored but the ion viscosity is retained (dashed-red), we find the instabilities are suppressed at high wavenumber ($k_y \approx 25m^{-1}$). However, the stabilization of the growing modes is found at $k_y \approx 81m^{-1}$ when we only consider the electron inertia term and drop the term coming from the ion viscosity. The

electron inertia is not relevant at these length-scales in the linear regime, however, it is important in saturating the growing modes of large amplitudes in the nonlinear regime.

A monotonic increase of the growth rate with the wavenumber (dashed-green) can be seen when we drop both the ion viscosity and the electron inertia terms. This case is similar to the standard two-stream fluid model [Fejer *et al.* 1975] that shows no cut-off for the type-I instability. However, the solid black line shows stabilization at large wavenumbers around $k_y = 11.5(m^{-1})$ when both the ion viscosity and electron inertia are included in the model.

A maximum growing mode at $k_y = 7.8(m^{-1})$ is equivalent to an irregularity of scale size less than a meter in the zonal direction. In the vertical direction we have the maximum growing mode at $k_z = 0$, and there are modes of positive growth rate at $k_z = 2.1(m^{-1})$, which is equivalent to 3 meters wavelength. Farely and Balsley [1973] found that the excitation of 3 meters wavelength waves requires a very large drift speed which is not possible in the equatorial electrojet region and they referred to Sudan's *et al.* [1973] theory, which attributed the generation of vertical structures of wavelength 3-meters or less in the equatorial electrojet to the cascade of energy to small scales.

The linear growth-rate for both types of instabilities that is derived in the standard fluid model by Fejer [1975] increase monotonically in contrast with the growth rate calculated numerically from our unified fluid model that includes both the ion viscosity and electron inertia terms. Our unified model produces a cut-off at high wavenumbers. The growth rate profile of the unified fluid model is similar to that of the kinetic model of type-I instability studied by Schmidt and Gary [1973] and Oppenheim *et al.* [1996], which was compared to the linear growth rate of the standard fluid model by Fejer [1975].

On the other hand, there is a decrease in the phase velocity found in our unified model compared to that which was estimated by the standard linear fluid model [Fejer 1975] as shown in figure(4). This decrease in the phase velocity at high wavenumbers is in agreement with the radar observation that shows a phase velocity limited to the acoustic speed of the ions inside the equatorial electrojet.

4.5. Type-I and Type-II Instabilities

The linear growth rate profile shows the presence of a transition from Type-II instability at small wavenumber ($< 0.1m^{-1}$) to the Type-I instability at large wavenumbers. For electron drift velocity less than the ion-acoustic speed we find that the growth rate maximum is located at the transition wavenumber ($\approx 0.1m^{-1}$) with a peak value that depends on the electron density scale length (L_n). Also, the level of the growth rate peak at the large wavenumbers, where type-I instability dominates, depends on both the electron drift speed (v_E) and the electron density scale length (L_n). Therefore, to include both instabilities, type-I and type-II, in our simulation we need both a small minimum wavenumber and a large box in k-space. We discussed the system initialization in the next section.

5. Nonlinear Regime and Results

Nonlinear evolution and saturation of Type-I and Type-II instabilities have been studied for several decades. The one-dimensional simulations that have been done by Sato and Tsuda [1967] and Rogister [1972] to study the gradient-drift (Type-II) instability were criticized by Sudan [1973] because they ignored the coupling between the waves propagate horizontally and vertically in the equatorial electrojet region. The saturation of

Farley-Buneman (Type-I) instability has also been studied in different types of simulations. Newman and Ott [1981] ran a fluid nonlinear simulation that shows the dominant wave to propagate in a direction that is different from the direction of the electron drift. A particle-in-cell (PIC) code was used by Machida and Goertz [1988] to model the dominant wave in a plane parallel to the geomagnetic field. This geometry ignores the nonlinear term, $\hat{b} \cdot \nabla \varphi \times \nabla n$ where \hat{b} is in the direction of the magnetic field, that is important for the saturation of Type-I instability.

Oppenheim *et al* [1996a] presented two-dimensional hybrid simulations that treat the electrons in the fluid regime and the ions kinetically to model the effects of Landau damping. The agreement between the radar/rocket spectra and the simulation spectra was presented by Oppenheim and Otani [1996b]. The hybrid simulation is able to reproduce the phase velocity during the saturated state similar to the drift velocity of the irregularities and its independence from the elevation angle. Also, the hybrid simulation shows the presence of a secondary Type-II instability in the absence of the electron density gradient as a result of the mode coupling. Otani and Oppenheim presented the mechanism of the saturation of Farley-Buneman (Type-I) instability in a series of papers [Otani and Oppenheim 1998, Otani and Oppenheim 2006]. Otani and Oppenheim attribute the saturation mechanism to the interaction between three modes in the system, and used a fluid model to reproduce some observed features from the echoes of the irregularities.

In 2008, Oppenheim *et al.* presented the results of a large-scale simulation from a fully kinetic simulator called Electrostatic Parallel PIC or EPPIC code. This is a high-resolution two-dimension simulation with (4096 x 4096) grid points that covers (160 m \times 160 m) space which is comparable to our simulation box. The simulation showed the

coupling between the linearly growing modes and the damped modes and included the electron and ion thermal effects. This simulation reproduced most of the measurements and features of Farley-Buneman turbulence with a phase velocity larger than the ion-acoustic speed. Later, Oppenheim and Dimant [2013] presented the first fully kinetic 3-D simulation results for the Farley-Buneman instability with the ionospheric condition at the aurora region. The simulator uses a sophisticated method in calculating the collision frequency of the ions and electrons, in addition to the anomalous heating of the electrons. The simulation was able to resolve the 1-5 meters waves during the transition region and the formation of a large structure at the saturation region. Also, it shows the role of the anomalous electron heating in reducing the phase velocity of the short waves to a value very close to the local ion-acoustic speed compared to the previous 2-D simulation. The electrons and ions thermal effects are out-of-scope of the current work in this paper and they will be considered in future work.

5.1. Nonlinear System Initialization

In our nonlinear simulation, we use the pseudospectral method to find the spatial derivatives of the fields in k-space and then integrate the three differential equations in the time domain using a sixth-order Runge-Kutta (RK6) method with periodic boundary conditions at all the boundaries of all fields. We solve our nonlinear system in a simulation box of size $100 \text{ m} \times 100 \text{ m}$ in the r-space with grid resolution 1024×1024 . This r-space grid is equivalent to $22 \text{ m}^{-1} \times 22 \text{ m}^{-1}$ in k-space (after removing the dealiasing region that is required by the nonlinear terms for spectral methods). We use 1024×1024 resolution to be able to include both types of instabilities (Type-II at $k_y \approx 0.1 \text{ m}^{-1}$ and Type-I at $k_y \approx 7.8 \text{ m}^{-1}$) in the simulation box of our dynamical system as we indicated earlier in

section (4) and show in figure(3).

The local values (where, $|kL_n| \gg 1$) around 105 km altitude for the physical quantities on March 2008; which is coincident with the deep minimum and a solar quiet (Sq) time of the last and unusual solar minimum conditions [Benevolenskaya and Kostuchenko 2013], with setting $v_E = 400m/s$ and $L_n = 6km$ are employed in the coefficients of the dynamical system equations. Woods *et al.* [2010] found the total solar irradiance in 2008 is much smaller than its value in the previous solar minimum in 1996, and the value of the solar radio flux index at this day is F10.7=69.9.

We initialize the plasma density, electric potential, and the ion velocity potential in k-space using the values of the eigenvectors calculated numerically in the eigenvalue problem at all the k_y and k_z values corresponding to positive growth rates as discussed in section(4), and we run the simulation for more than 1 second with $10 \mu s$ time step.

5.2. Spectral Analysis of Electron Density

In the nonlinear run we evolve the perturbed normalized quantities $(\delta\tilde{n}, \delta\tilde{\varphi}, \delta\tilde{\chi})$ in k-space over time to check the transition from the region of linear dominance to the region of nonlinear dominance and end in the saturated state of the simulation. Snapshots of the energy spectrum of the plasma density are shown in figure(5) at different stages of the simulation. For context, the reader is also referred to figure(3) (which shows the range of linear instability), and figures(6-8) (which show the time evolution of the density perturbations).

The first panel in figure(5) shows the energy spectrum of the plasma density in the linear growth phase with more energy content at small k-values in the horizontal and vertical directions. In the second panel, the energy is concentrated at low k_z and shifts to

higher k_y to damp linearly after generating waves of sub-meter wavelengths. Panels three through five demonstrate the transition from initial nonlinear stabilization to fully saturated turbulence. The third panel ($t = 0.53$ s) represents a point of transient saturation, as can be seen in figure(10). At this point, the energy is largely concentrated in the small type-I scale range. In panel four, the dominant scales are reversed during the transition to the final saturated state. Here the energy is concentrated at large type-II scales, with comparatively less energy at small scales. In the fifth panel, the final nonlinear balance is achieved with two distinct scales having energy apportioned quite evenly between them. These two dominant scales, however, are embedded in broadband turbulence, as can be seen from the significant energy observed over the entire instability range (e.g., in the intermediate $k_y = 2.0 - 7.0$ range).

The onset of the nonlinearity dominance in the transition region is coincident with the generation of long structures of the plasma irregularities in the vertical direction with scale length of 40 meters, see figure (7). In addition, we attribute the generation of the 3 meter scale waves in the vertical direction to the cascade energy transfer from the long structures at small wavenumbers to the short irregularities at the large wavenumbers which is consistent with the theory of Sudan *et al.* [1973] for the generation of small-scale irregularities in the equatorial electrojet.

This complex nonlinear interplay between the two scales and the back and forth exchange of energy between them will be studied in detail in future work using nonlinear energy transfer functions.

5.3. Instabilities Evolution, Coupling, and Saturation

Many of the features described in the previous section can also be directly observed in real-space contour plots. The upward (downward) drift of the low-density (high-density) plasma is shown in figure(6) during the linearly growing phase of the simulation. The vertical drift velocity is found from successive frames to be around 50-70 m/s. The plasma is broken horizontally into small-scale waves of 1-3 meters in wavelength.

Figures(7 and 8) show snapshots of the plasma density fluctuations at $t = 0.6$ s (during the initial saturation phase) and $t = 1.0$ s (during the final saturated phase), respectively. The multi-scale nature of the turbulence is evident in the East-West direction in both figures, with prominent features visible at ~ 1 m that are embedded in structures with ~ 10 m scale. In the vertical direction, the fluctuations exhibit a stark change during this transition to fully developed turbulence. The vertical structures are very large scale $\sim 20 - 40$ m at $t = 0.6$ s, but are reduced to $\sim 1 - 3$ m at $t = 1.0$ s. At this point, the simulation box is filled with small-scales structures embedded both vertically and horizontally in the long-scale irregularities of Type-II instabilities. The small-scale vertical structures can be considered as the formation of secondary type-I instabilities in the vertical direction and is consistent with the energy cascade theory [Sudan *et al.* 1973] to small vertical scales.

A closer look at the turbulence in the plasma density under the solar-maximum condition (March 1987) is shown in figure(9). The left-panel shows the long-structures at $t = 0.75$ s which is right-shifted in time with respect to the transition region under the solar-minimum condition as we discussed in the next section. These long-structures fill the box with a few small-scale structures. At $t = 1.2$ s, the perturbation in density is saturated and we see in the right-panel of figure(9) many small-structures of 1-3 meter scale-length. The structure of the plasma density during the growing-, transition-, and

saturation-phases of the simulation is identical under different solar conditions and only the saturation level of the perturbation is different.

Watching successive frames of the density evolution during the saturation states shows that the downward and upward drifts are not in a straight vertical direction, but they drift with an inclination to the horizontal direction which is parallel to the direction of $\underline{E} \times \underline{B}$ plasma drifts. Oppenheim and Otani [1996] called this motion toward the corners of the simulation box "a bent of the primary waves," and they attributed it to the decrease in the linear growth-rate for the primary waves of $k_z \neq 0$ to a value that is below its value at $k_z = 0$ in the linear regime of the simulation. This feature can be seen from the vertical profile of the growth rate.

5.4. Turbulence in Electron Density

A comparison between the temporal variation of the plasma density during the condition of solar maximum on March 1987 (blue-line) and the condition of solar-minimum on March 2008 (red-line) is shown in figure(10). The top-panel shows the maximum perturbation in the plasma density, however the bottom-panel shows the standard-deviation of the perturbed density as a function of time.

The standard-deviation shows distinctly the three domains of the simulation: linear, transition and saturation. The evolution time required in the simulations in the growing phase under the solar-maximum conditions is longer than the corresponding time under the solar-minimum conditions. Also, the level of the standard-deviation of the saturated perturbed plasma density is higher under the solar-maximum conditions ($\sigma_{\delta n} = 3.0\%$) than the solar-minimum conditions ($\sigma_{\delta n} = 1.7\%$) with a $\Delta t = 0.1$ s difference between their start of the saturation region in the simulation.

Under the solar-minimum condition, the perturbation in the electron density increases to 12% of the background density during the transition region before it goes back to 7% in the saturation region as a result of the strong coupling between the primary and secondary waves in the nonlinear saturation regime.

This is below the expected 10-12% perturbations found in both the Rocket and the Radar Observations [Balsley and Farely 1971, Kudeki *et al.* 1987, Pfaff *et al.* 1997, Hysell *et al.* 2007]. Our interpretation of the low level of plasma density perturbations is the result of the low solar radio flux accompanied by the unusual solar minimum conditions and the solar quiet condition employed in this simulation [Benevolenskaya and Kostuchenko 2013, Woods *et al.* 2010].

When we examined the dynamic system under solar-maximum conditions we found that the temporal variation of the perturbed density during the saturation region shows a maximum much higher than the 7% found during the solar-minimum conditions. The perturbation in the electron density increases to 25% of the background density during the transition region before it goes back to 15% in the saturation phase. In a following paper, we are going to examine the effect of the background electric field and density-gradient scale-length on the maximum value of the perturbed density.

5.5. Perturbed Electric Fields

The maximum perturbed electric field in the zonal and vertical directions are shown in the upper and lower panels of figure(11), respectively. The zonal component of the perturbed electric field grows to 140 mV/m before it saturates at 80 mV/m under the solar-maximum conditions which is double its saturation value under the solar-minimum conditions. Similarly, the vertical electric field saturates at a larger value (35 mV/m)

compared to the solar minimum saturation value (15 mV/m). The difference in the perturbed field between the solar maximum and solar minimum is directly related to the level of the perturbed density under these different conditions which is discussed in the previous subsection.

The root-mean-squares (rms), which are measurable quantities, for the perturbed electric field in the zonal (solid-lines in upper-panel) and vertical (solid-lines in lower-panel) directions are shown in figure(12). While the magnitude of the rms of the zonal perturbed electric field in the saturation regime reaches 15 mV/m during the solar maximum conditions, it does not exceed 8 mV/m under the solar minimum conditions. On the other hand, the rms value ($\delta E_z = 3.0$ mV/m) of the perturbed vertical electric field under the solar-maximum conditions is almost double its value ($\delta E_z = 1.7$ mV/m) under the solar-minimum conditions.

The simulation results of the magnitude of the zonal and vertical perturbed fields under the ionosphere conditions of March 1987 shows a good agreement to the measured rocket data in the CONDOR campaign of the perturbed electric field in the zonal direction.

5.6. Plasma Fluxes Asymmetries

The "east-west" zonal and "up-down" vertical components of the perturbed electric field are shown in the upper and lower panels of figure(12), respectively, during the solar-maximum (red) and solar-minimum (blue) conditions. While the solid lines represent the rms of total perturbed electric fields, the dotted and dashed lines represent the rms of the westward (upward) and eastward (downward) perturbed components in the zonal (vertical) directions, respectively.

These zonal and vertical components of the electric field give rise to Pedersen drifts

along its direction and Hall drifts in a direction perpendicular to the plane containing both the electric field and the magnetic field as a result of the $\mathbf{E} \times \mathbf{B}$ drift. The large ratio between the Hall and Pedersen conductivities makes the effect of the Hall current more important in the equatorial electrojet region. In turn, the difference in the Hall currents in the zonal and vertical directions gives rise to an asymmetry in the drift velocities and density fluxes in both directions.

The large difference between the upward and the downward components of the perturbed electric field is common in all phases of simulation and causes an "east-west" asymmetry in the drift velocity. Patra *et al.* [2005] reported the first observations verifying the "east-west" velocity asymmetry found in Type-II echoes using a 18 MHz radar located at Thumba Equatorial Rocket launching Station (TERLS), Trivandrum, India. Patra *et al.* [2005] attributed the "east-west" velocity asymmetry to the large-scale primary waves that give rise to a large upward plasma drift. However, we find the "east-west" asymmetry exists even after the breaking-up of the large-scale vertical waves into smaller-scale structures. Thus, we consider the "up-down" asymmetry of vertically perturbed electric field, which is responsible of the zonal Hall drifts, to be the cause of the "east-west" velocity asymmetry.

On the other hand, the asymmetry in the vertical fluxes produces echoes of different strengths in the spectrograms from the AMISR prototype at Jicamarca as reported by Hysell *et al.* [2007] and studied by Fejer *et al.* [1976], Farley *et al.* [1978], and Kudeki *et al.* [1985]. The Hall drifts in the vertical direction do not show large asymmetry because of the very small difference between the zonal components of the perturbed field as shown in the upper panel of figure(12). The large difference between the zonal components can

only be found in the presence of large-scale structures during the transition phase of the simulation, under the condition of solar maximum, and then decreases as it goes deep in the saturation phase with the "break-up" of the large-scale irregularities into small-scale structures. However, the large difference in the Pedersen drifts may play a role in causing the asymmetry in the density flux along the vertical direction.

5.7. Phase Velocity of Plasma Irregularities

The plasma density in the zonal direction as a function of time is shown in figure(13). The inverse Fourier transform of the density spectrum is taken for all k_y values of $k_z=0$ (m^{-1}) for all time steps in the saturation state of the simulation. We can see small-scale waves of Type-I superimposed on the large-scale waves of Type-II. The phase velocity of the small-scale waves has a value of 330 (m/s) and drifts westward. This value of phase velocity is very close to the ion-acoustic speed (318-323 m/s) calculated from the ionosphere background data. So, the phase velocity of the irregularity waves is limited to the ion-acoustic speed at the core of the electrojet. This result shows a good agreement with the radar and rocket observations that limit the speed of the plasma irregularities in the ionosphere E-region to the acoustic speed of ions and show them propagating in the westward direction [Farely and Balsley 1973, Kudeki *et al.* 1987].

6. Summary and Conclusion

The temporal and spatial evolution of the plasma density, electric potential, and ion velocity potential are studied linearly and nonlinearly in a two-dimensional fluid model. Our unified fluid model considers both ion viscosity and electron inertia. The dominant nonlinear terms $[\delta\tilde{\varphi}, \delta\tilde{n}]$ and $[\delta\tilde{\varphi}, \nabla^2\delta\tilde{\varphi}]$, are responsible for the coupling between Type-I

and Type-II fluctuations and drive the dynamic system to the statistically steady state.

In our unified model, the electron inertia, which has been ignored in the earlier models, adds the polarization drift to the dynamic system and is important for the nonlinear coupling between different modes and the saturation of growing modes of small-scale structures. The ion viscosity models Landau damping, which, in contrast with kinetic models, is not included in fluid treatments.

The linear results also show that the ion viscosity and electron inertia are important for stabilizing the large wavenumbers around 3 meter scale sizes in the vertical direction and less than a meter in the horizontal direction. The unified fluid model linear growth rate is comparable to the growth rate calculated with a kinetic model by Gary and Schmidt [1973] and a hybrid model by Oppenheim *et al.* [1996] for the Farley-Buneman (Type-I) instability. The linear phase velocity predicted from our unified model is smaller than that obtained from the standard two-stream fluid model in such a way that is generally consistent with the observed values of the phase velocity and close to the ion-acoustic speed.

The altitude-dependence of the growth rate profile shows the role of Type-I and Type-II instabilities in exciting the irregularities in the E-region between 90-120 km as suggested from the rocket data studied by Pfaff [1987]. Type-II instabilities dominate between 90-103 km where the plasma is very collisional and electron drifts are too small to excite Type-I instability. However, Type-I instability dominates between 110-115 km in a region of negative gradients that suppresses Type-II instability. The coupling between Type-I and Type-II instabilities takes place at the core of the electrojet region between 103-110 km where the maximum growth rate is extending over a wide range of wavenumbers.

The time-series of the spectrum of the density perturbation shows the back and forth exchange of energy between plasma irregularities of different scales. This exchange of energy can be considered to be a verification of the Sudan *et al.* [1973, 1983] theory of cascade energy transfer to structures of 3 meters scale in the vertical direction. The perturbed density spectrum exhibits the coupling between Type-I and Type-II instabilities and shows the generation of long-scale structures in the vertical direction. It also demonstrates how the energy is transferred back from the large-scale perturbed density structures excited by type-II modes to the small-scale irregularities exhibiting type-I features. The plasma density spectrum shows an even distribution of energy between the large-scale structures (small wavenumbers) that produced type-I modes and the small-scale structures (large wavenumbers) that produced by type-II modes. The energy content of the irregularities of scale-length less than a meter in the vertical direction is small, which explains the difficulties to detect them by coherent scattered radars [Farley and Balsley 1973]. In addition, the embedding of the small-scale structures in the large-scale structures demonstrates the difficulty to observe the long-scale structures of type-II while type-I instabilities are excited.

Our nonlinear model is able to reproduce a number of features of rocket measurements and radar observations under different solar conditions such as: (1) a saturation of the density perturbation between 7-15%, (2) root-mean-square values of the horizontal component ($\delta E_y = 8.7-15$ (mV/m)) and vertical component ($\delta E_y = 1.7-3$ (mV/m)) of the perturbed electric field, (3) a linear and nonlinear reduction of the phase velocity of the horizontal westward irregularities to values less than or equal the ion-acoustic speed, (4) an asymmetry in the plasma fluxes in the vertical direction as a result of an asymmetry

of the perturbed zonal electric field components, (5) an asymmetry in the plasma drifts in the horizontal direction as a result of an asymmetry of the perturbed vertical electric field components, (6) a break-up of the large-scale vertical plasma structures into small-scale structures of 3 meters and less in the saturation state, (7) an inclination of the small structures drift toward the corners of the simulation box as a result of the vertical up (down) drifts of the depletion (enhanced) density regions due to Type-II instability.

The low-level of fluctuations of the electron density and the small eastward zonal perturbed electric field are attributed to the solar quiet (Sq) and unusual minimum conditions with low total solar irradiance on March 2008.

In conclusion, this unified fluid model is able to reproduce comparable results in the linear regime to the kinetic theory for both the growth rate stabilization and the reduction in phase velocity. It also exhibits quantitatively the coupling between Type-I and Type-II instabilities excited in the equatorial electrojet region and the cascade transfer of energy to small structures as proposed by Sudan [1973]. The excitation of secondary Type-I instabilities from Type-II is verified and seen from the spectrum of the perturbed density at 105 km altitude. Finally, the nonlinear results match most of the radar observations and rocket measurements.

Employing an advanced parallel computing technique such as *Message Passing Interface (MPI)* with this stable fluid model will ensure the retrieve of all the E-region features with a large-scale simulation that covers equatorial electrojet layer.

Acknowledgments. This work is supported by the National Science Foundation grant AGS-0964692 to the University of Texas at Austin. The first author has been partially

supported by Ain Shams University, Cairo, Egypt and the Egyptian Government to pursue his Ph.D. studies at the University of Texas at Austin.

References

- Baker, W.G., and Martyn, D.F. (1953). Electric Current in the Ionosphere, I, The Conductivity, Philos. Trans. R. Soc. London, Ser. A, 246, 281.
- Balsley, B. B. (1969), Some characteristics of non-twostream irregularities in the equatorial electrojet, J. Geophys. Res., 74(9), 2333-2347.
- Balsley, B. B., and D. T. Farley (1971), Radar studies of the equatorial electrojet at three frequencies, J. Geophys. Res., 76(34), 8341-8351.
- Balsley, B. B., and D. T. Farley, (1973), Radar studies of the equatorial electrojet at three frequencies, J. Geophys. Res., 78, 7471.
- Benevolenskaya, E. E., and I.G. Kostuchenko, (2013), The Total Solar Irradiance, UV Emission and magnetic Flux during the Last Solar Cycle Minimum, Journal of Astrophysics, Vol. 2013, Article ID 368380.
- Bilitza D., and Reinisch, B. (2008), International Reference Ionosphere 2007: Improvements and new parameters, J. Adv. Space Res., 42, 4, pp. 599-609.
- Bowles, K.L., Balsley. B.B., Cohen, R. (1963). Field-aligned E region irregularities identified with acoustic plasma waves, J. Geophys. Res., 68, 2485.
- Buneman, O. (1963). Excitation of field-aligned sound waves by electron streams. Phys. Rev. Lett., 10, 285.
- Cohen, R., and Bowles, K.L. (1967). Secondary irregularities in the equatorial electrojet. J. Geophys. Res. 72, 885.

Farley, D.T. (1963). A plasma instability resulting in field-aligned irregularities in the ionosphere. *J. Geophys. Res.*, 68, 6083.

Farley, D. T., and B. B. Balsley (1973), Instabilities in the equatorial electrojet, *J. Geophys. Res.*, 78,227.

Farley, D.T. (2009). The equatorial E-region and its plasma instabilities: a tutorial. *Ann. Geophys.*, 27, pp. 1509-1520.

Fejer, B.G., Farley, D.T., Balsley, B.B., and Woodman, R.F. (1975). Vertical structure of the VHF backscattering region in the equatorial electrojet and the gradient drift instability. *J. Geophys. Res.*, 80, 1313.

Fejer, B. G., D. T. Farley, B. B. Balsley, and R. F. Woodman, (1976), Radar observations of two-dimensional turbulence in the equatorial electrojet, *J. Geophys. Res.*,81, 130.

Fejer, B.G., and Kelley, M.C. (1980), "Ionospheric irregularities", *Rev. of Geoph.and Space Phy.*, Vol.18, No.2, pp. 401-454.

Forbes J.M. (1981). The Equatorial Electrojet, *Rev. Geophy. and Space Phy.*, Vol 19, No. 3, pp. 469-504.

Hanuisse, C., and M. Crochet (1981), 5-50 m wavelength plasma instabihties in the equatorial electrojet, 2, Two-stream conditions, *J. Geophys. Res.*, 86, 3567.

Hoh, F.C. (1963). Instability of Penning-type discharge. *Phys. Fluids*, 6, 1184.

Hysell, D.L., Drexler, J., Shume, E.B., Chau, J.L., Scipion, D.E., Vlasov, M., Cuevas, R., and Heinselman, C. (2007). Combined radar observations of equatorial electrojet irregularities at Jicamarca. *Ann. Geophys.*, 25, 457473.

Horton, W., and Hasegawa A. (1994), Quasi-two-dimensional dynamics of plasmas and

fluids, Chaos, pp. 227-251.

Horton, W., and Ichikawa Y. H. (1996), Chaos and Structures in Nonlinear Plasmas, World Scientific, Singapore.

Kamenetskaya, G. Kh. (1971), Quasi-linear theory of the formation of inhomogeneities in the equatorial electrojet, Geomagn. Aeron., 11, 71-75.

Kaw, P. K., (1972), Wave propagation effects on observation of irregularities in the equatorial electrojet, J. Geophys. Res., 77, 1323-1326.

Knox, F. B., A contribution to the theory of the production of field-aligned ionization irregularities in the equatorial electrojet, J. Atmos. Terr. Phys., 26, 239-249, 1964.

Kelley, M.C. (2009). The Earth's Ionosphere, Plasma Physics and Electrodynamics, 2nd edition, Amsterdam ; Boston : Academic Press, 2009.

Kudeki, E., D. T. Farley, and B. G. Fejer (1982), Long-wavelength irregularities in the equatorial electrojet, Geophys. Res. Lett., 9, 684.

Kudeki, E., D. T. Farley, and B. G. Fejer (1985), Theory of spectral asymmetries and nonlinear currents in the equatorial electrojet, J. Geophys. Res., 90,429.

Kudeki, E., Fejer, B.G., Farley, D.T., and Hanuise, C. (1987). The CONDOR Equatorial Electrojet Campaign: Radar results, J. Geophys. Res., 92, 13,561.

Kudeki, E., and Farley, D.T. (1989). Aspect Sensitivity of Equatorial Electrojet Irregularities and Theoretical Implications, J. Geophys. Res., 94, A1, 426-434.

Lu F., Farley, D.T., and W.E. Swartz (2008). Spread in aspect angles of equatorial E region irregularities, J. Geophys. Res., 113, A11309, doi:10.1029/2008JA013018.

Machida, S., and C. K. Goertz (1988), Computer simulation of the Farley-Buneman instability and anomalous electron heating in the auroral ionosphere, J. Geophys. Res.,

93, 9993.

Maeda, K., T. Tsuda, and H. Maeda, Theoretical interpretation of the equatorial sporadic E layers, Rep. Ionos. Space Res. Jap., 17, 3, 1963.

Newman, A. L., and E. Ott (1981), Nonlinear simulations of type I irregularities in the equatorial electrojet, J. Geophys. Res., 86, 6879.

Oppenheim, M. M., N. F. Otani, and C. Ronchi (1996), Saturation of the Farley-Buneman instability via nonlinear electron $E \times B$ drifts, J. Geophys. Res., 101.

Oppenheim, M. M., and N. F. Otani (1996), Spectral characteristics of the Farley-Buneman instability: simulations versus observations, J. Geophys. Res., 101.

Oppenheim, M. M., Y. Dimant, and L. P. Dyrud (2008), Large-scale simulations of 2-D fully kinetic Farley-Buneman turbulence, Ann. Geophys., 26, 543-553.

Oppenheim, M. M. and Y. S. Dimant (2013), Kinetic simulations of 3-D Farley-Buneman turbulence and anomalous electron heating, J. Geophys. Res. (Space Physics), 118, 1306-1318, doi:10.1002/jgra.50196.

Otani, N.F., Oppenheim, M.M., (1998). A saturation mechanism for the Farley-Buneman instability. Geophysical Research Letters 25, 1833-1836.

Otani, N. F. and Oppenheim, M. (2006), Saturation of the Farley-Buneman instability via three-mode coupling, J. Geophys. Res. (Space Physics), 111, 3302, doi:10.1029/2005JA011215.

Patra, A. K., Tiwari, D., Devasia, C. V., Pant, T. K., and Sridharan, R.: East-west asymmetries of the equatorial electrojet 8.3m type-2 echoes observed over Trivandrum and a possible explanation, J. Geophys. Res., 110, A11305, 2005.

Pfaff, R. F., M. C. Kelley, E. Kudeki, B. G. Fejer, and K. Baker (1987a), Electric field

and plasma density measurements in the strongly driven daytime equatorial electrojet,
 1, The unstable layer and gradient drift waves, J. Geophys. Res., 92, 13578.

Pfaff, R.F., Kelley, M.C., Kudeki, E., Fejer, B.G., and Baker, K.D. (1987b). Electric
 field and plasma density measurements in the strongly driven daytime equatorial
 electrojet. 2 Two-stream waves, J. Geophys. Res., 92, 13,597.

Pfaff Jr., R.F., Acua, M.H., Marionni, P.A., Trivedi, N.B., (1997a). DC polarization
 electric field, current density, and plasma density measurements in the daytime
 equatorial electrojet. Geophysical Research Letters 24, 16671670.

Pfaff Jr., R.F., Marionni, P.A., Swartz, W.E., (1997b). Wavevector observations of
 the two-stream instability in the daytime equatorial electrojet. Geophysical Research
 Letters 24, 16711674.

Reid, G. C. (1968), The formation of small-scale irregularities in the ionosphere, J.
 Geophys. Res., 73(15), 1627-1646.

Rogister, A., and N. D'Angelo (1970), Type II irregularities in the equatorial electrojet,
 J. Geophys. Res., 75(19), 3879-3887.

Rogister, A. (1971), Nonlinear theory of type I irregularities in the equatorial electrojet,
 J. Geophys. Res., 76(31), 7754-7760.

Rogister, A. (1972), Nonlinear theory of cross-field instability with application to the
 equatorial electrojet, J. Geophys. Res., 77 (16), 2975-2981.

Rogister, A., and E. Jamin (1975), Two-dimensional nonlinear processes associated
 with "Type I" irregularities in the equatorial electrojet, J. Geophys. Res., 80, 1820-1828.

Richmond, A.D. (1973). Equatorial electrojet. I. Development of a model including
 winds and instabilities. J. Atmos. Terr. Phys., 35, 1083.

Rishbeth, H. (1997). The Ionospheric E-layer and F-layer dynamos - a tutorial review.
J. of Atmos. and Solar-Terr. Phys. Vol.59, No.15.

Ronchi, C., Similon, P.L., and Sudan, R.N. (1989). J. Geophys. Res., Vol.94, No.A2,
p.p.1317-1326.

Sato, T., and T. Tsuda (1967), Computer study on nonlinear cross-field instability,
Phys. Fluids, 10, 1262.

Simon, A. (1963). Instability of a partially ionized plasma in crossed electric and
magnetic fields. Phys. Fluids, 6, 382.

Schmidt, M. J., and S. P. Gary (1973), Density gradients and the Farley-Buneman
instability, J. Geophys. Res., 78, 8261.

Skadron, G., and J. Weinstock, (1969), Nonlinear stabilization of a two-stream plasma
instability in the ionosphere, J. Geophys. Res., 74, 5113-5126.

Sudan R.N., Akinrimisi, J., and Farley, D.T. (1973). Generation of small-scale irregu-
larities in the equatorial electrojet, J. Geophys. Res., Vol.78, No.1, pp. 240-248.

Sudan, R. N. (1983a), Nonlinear theory of type I irregularities in the equatorial
electrojet, J. Geophys. Res., 88, 40.

Sudan R.N. (1983b). Unified theory of type-I and type-II irregularities in the equatorial
electrojet, J. Geophys. Res., Vol.88, No.A6, pp. 4853-4860.

Sudan R.N., Gruzinov A.V., Horton W., and Kukharkin N. (1997). Convective
turbulence in weakly ionized plasma, Physics Reports, Vol.283, No.1, pp. 95-119.

Weinstock, J., and A. Sleeper (1972), Nonlinear saturation of 'type I' irregularities in
the equatorial electrojet, J. Geophys. Res., 77(19), 3621-3624.

Wernik, A.W., Secan, J.A., Fremouw, E.J. (2003). "Ionospheric Irregularities and

757 Scintillation”, Adv. Space Res., Vol.31, No.4, pp.971-981.

758 Woods, T.N., S. Cranmer, T. Hoeksema, and J. Khol (2010). ”Irradiance Variations
759 during this Solar Cycle Minimum,” in SOHO-23: Underswtanding a Peculiar Solar
760 Minimum, Eds., vol. 428 of *ASP Conference Series*, p. 63.

761

Table 1. Ionosphere Background Parameters

Quantity	Symbol	Unit	Solar Maximum	Solar Minimum
Electron Density	N_e	m^3	1.52×10^{11}	1.60×10^9
Electron Temperature	T_e	$^{\circ}K$	192.1	191.1
Ion Temperature	T_i	$^{\circ}K$	192.1	191.1
Magnetic Field	B_o	T	3.7×10^{-5}	3.5×10^{-5}
Ion Acoustic Speed	C_s	m/s	318.5	323.5
Electron Thermal Speed	v_{te}	m/s	5.4×10^4	5.4×10^4
Ion Thermal Speed	v_{ti}	m/s	225.2	228.5
Electron-Neutral Collision Frequency	ν_{en}	s^{-1}	2.3×10^4	2.4×10^4
Electron-Neutral Collision Frequency	ν_{in}	s^{-1}	3.2×10^3	2.8×10^3
Electron Gyro-Frequency	ω_{ce}	s^{-1}	6.5×10^6	6.1×10^6
Ion Gyo-Frequency	ω_{ci}	s^{-1}	113	110
Electron Larmor Radius	ρ_e	m	8.3×10^{-3}	8.8×10^{-3}
Ion Larmor Radius	ρ_i	m	2	2

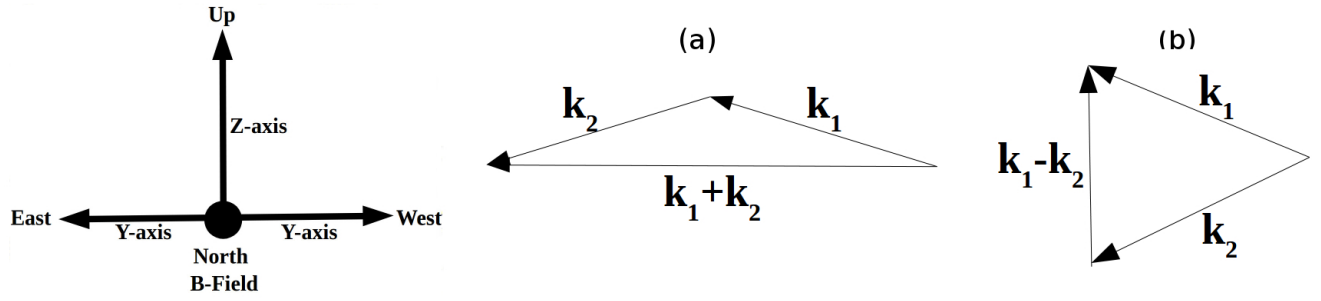


Figure 1. The dynamic system geometry. The y-axis is parallel to the zonal direction and the z-axis is points upward. The magnetic field is out of the paper and parallel to the x-axis. The possible unstable linear-modes coupling with forward (a) or inverse (b) cascade energy transfer.

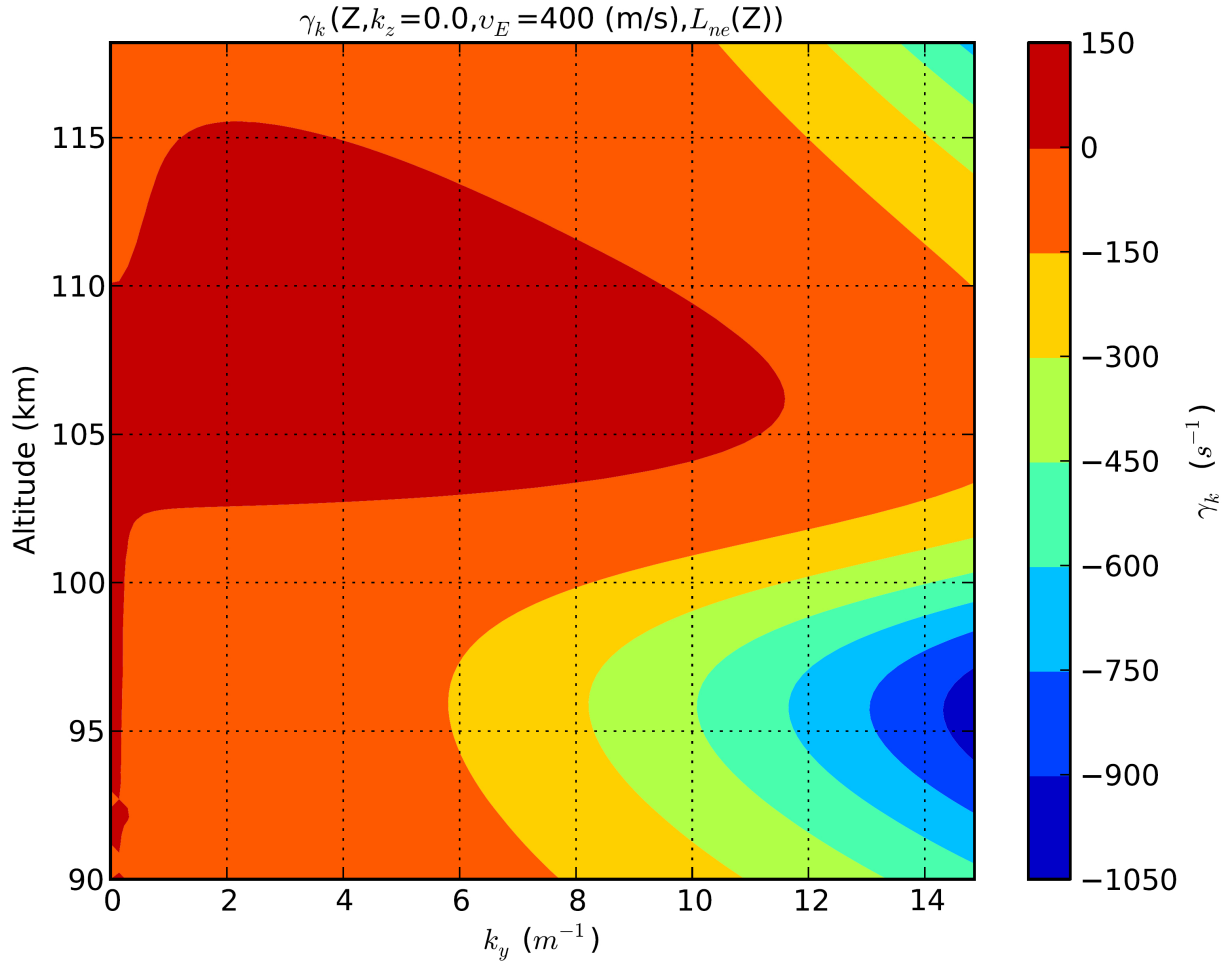


Figure 2. The growth-rate profile of the unified model as a function of altitude and horizontal wavenumber (k_y). It shows the dominance of Type-II instability at low altitudes up to the coupling region between Type-I and Type-II instabilities between 100-110 km. Above 110 km, Type-I instability dominates and Type-II instability disappears as a result of the reverse of the electron density scale length sign to be negative at that region.

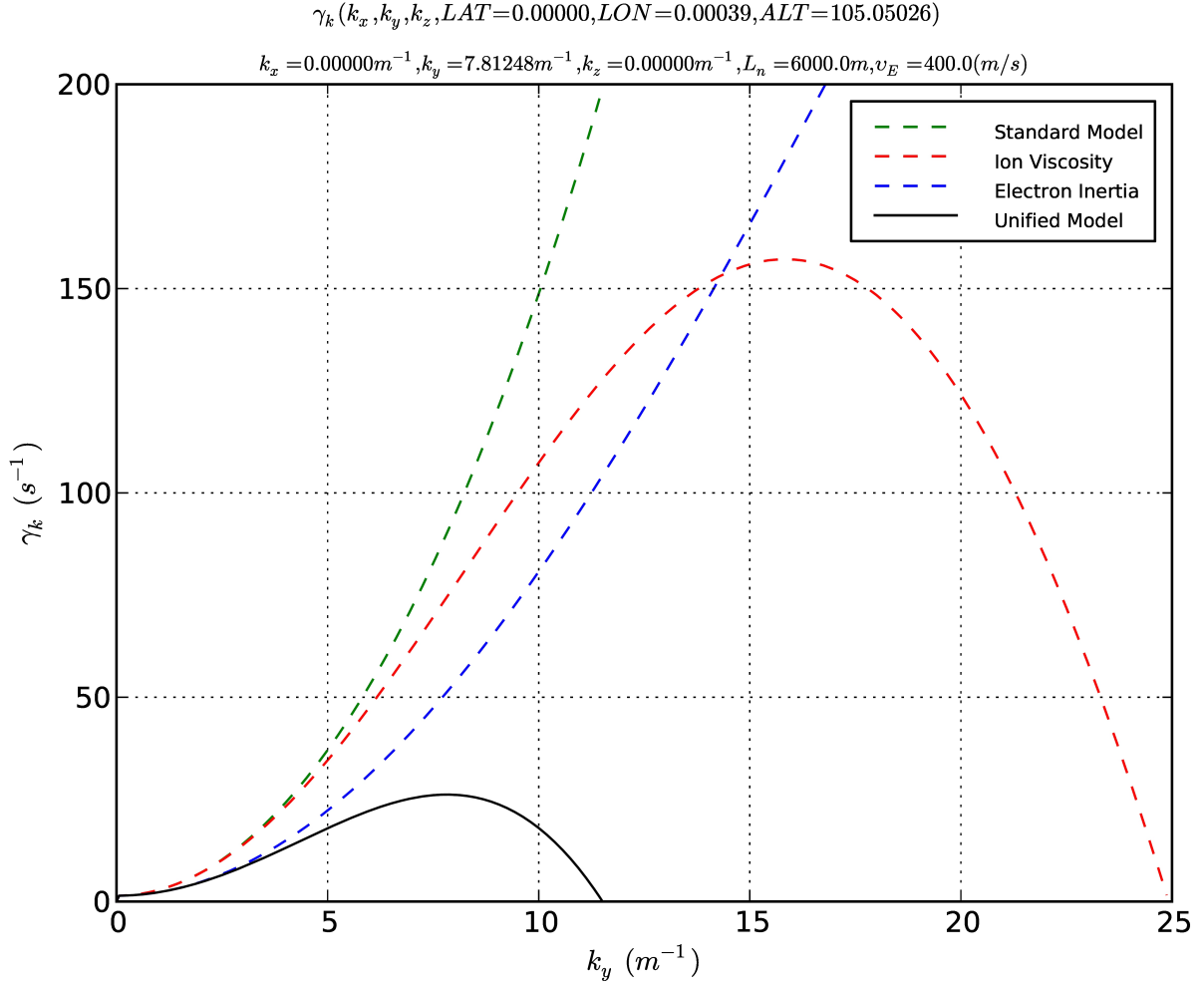


Figure 3. A comparison between the growth-rate, $\gamma_k(k_y)$, in the standard two-stream model (dashed-green) and the unified model with including both the ions viscosity and the electrons inertia (solid-black), absence of ions viscosity (dashed-blue), and absence of electrons inertia (dashed-red).

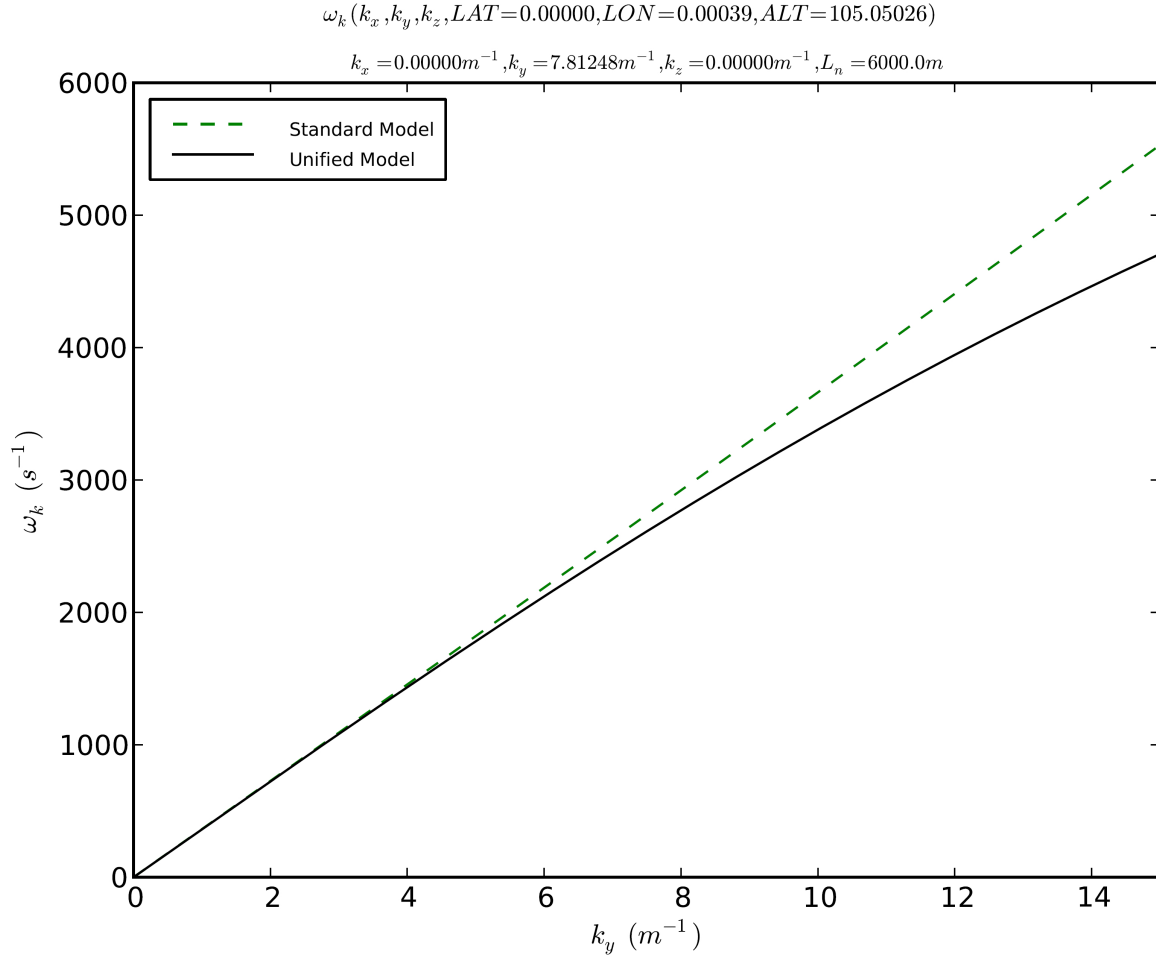


Figure 4. A comparison between the real-frequency, $\omega_k(k_y)$, profile of the standard two-stream model (dashed-green) and the unified model with including both the ions viscosity and the electrons inertia (solid-black). The unified model gives smaller phase velocity than the standard two-stream model.

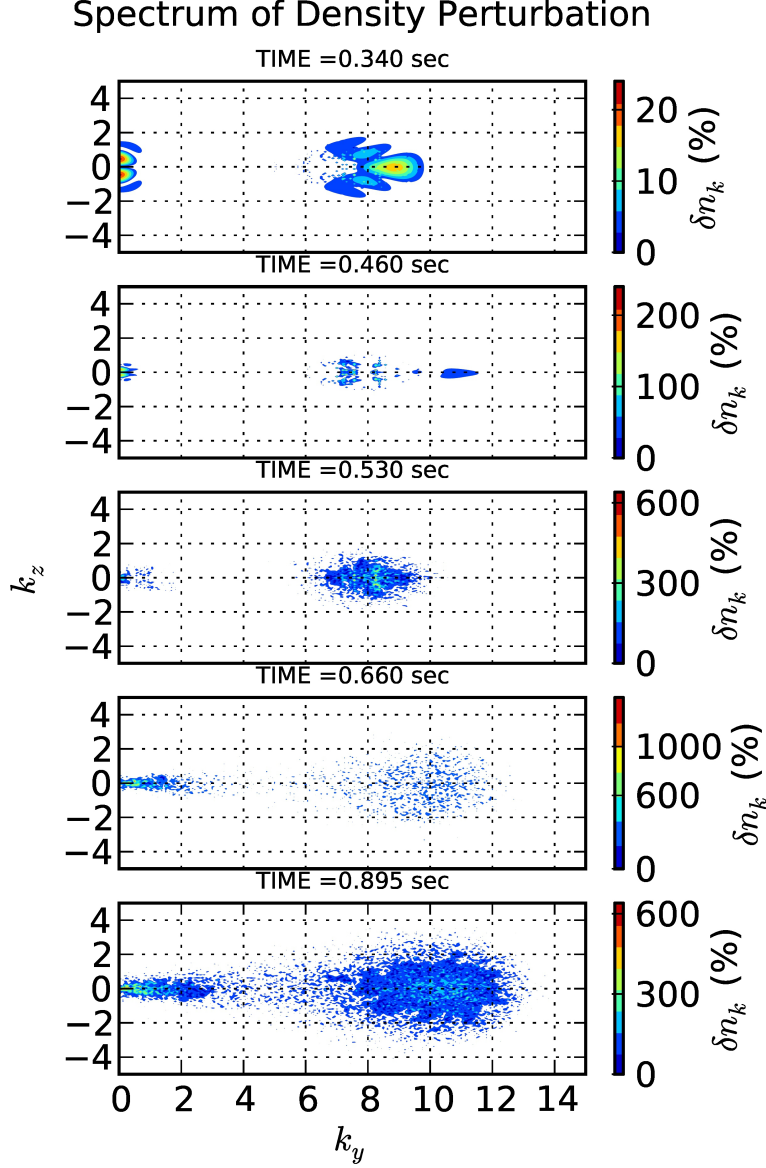


Figure 5. The Energy Spectrum of the Perturbed Electron Density at different states of the simulation. The top panel shows the energy spectrum of the available modes accumulates at two peaks for two types of instabilities at low- and high- k values. The second panel shows the growth of modes at higher wavenumbers. The modes of k -values with negative growth-rate decay linearly. The third panel shows the state of energy distribution during the transition region. The fourth and the fifth panels show the redistribution of energy over the modes at all wavenumbers which verifies the nonlinear coupling between different modes in the system.

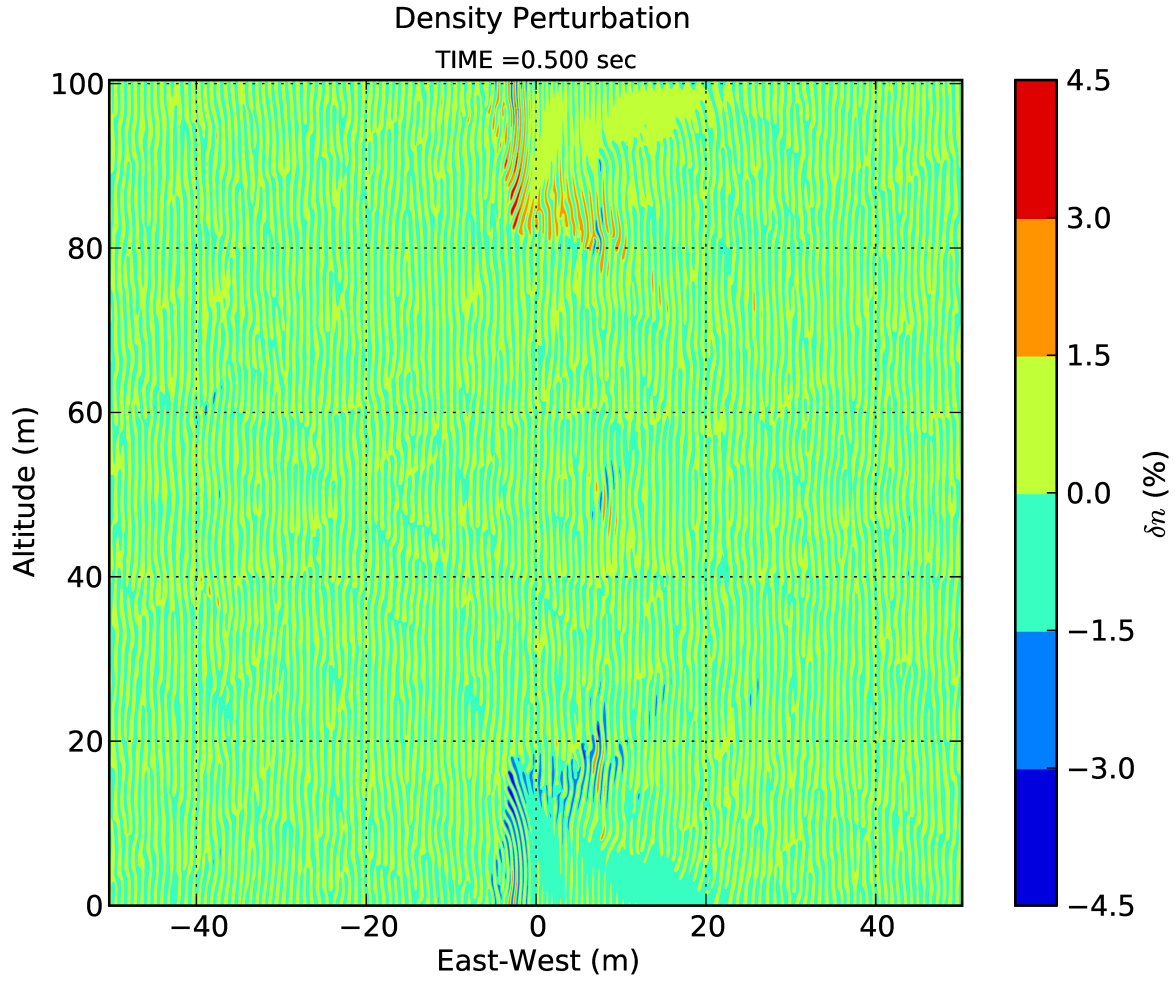


Figure 6. The Evolution of the Perturbed Electron Density at $t = 500$ ms during the dominance of the linear terms on the simulation under the solar-minimum conditions. It shows the downward drifts of the high-density plasma and upward drifts of low-density plasma.

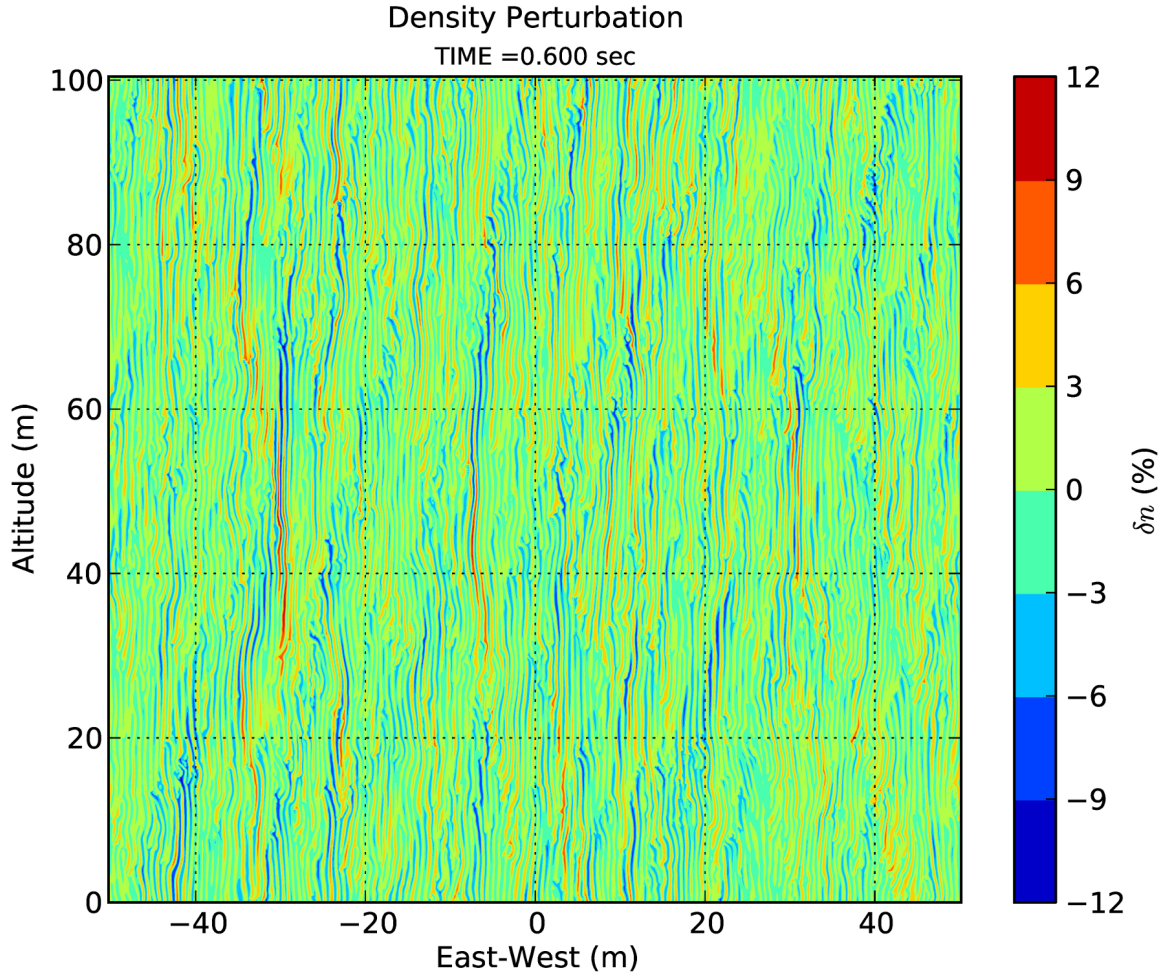


Figure 7. The Perturbed Electron Density at $t = 600$ ms during the transition from the linear to the saturation phase of the simulation under the solar-minimum conditions. It shows large size structures of plasma densities that are drifting horizontally and vertically at different velocities with maximum perturbation of 12%.

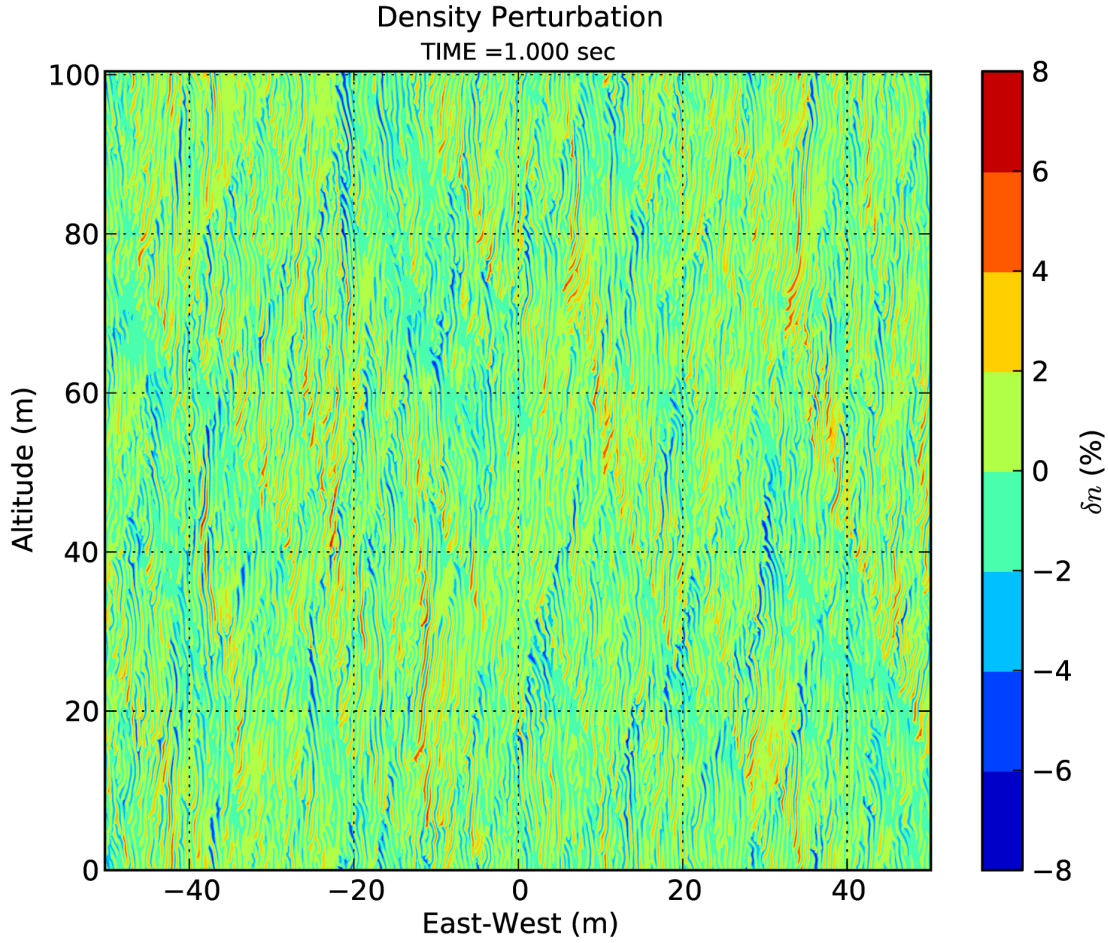


Figure 8. The Perturbed Electron Density at $t = 1000$ ms the saturation state of the simulation reaches 8% relative to the background density under the solar-minimum conditions. It shows the very small structures embedded in the larger structures that are seen in the transition phase as a result of the coupling between Type-I and Type-II instabilities in the saturation state.

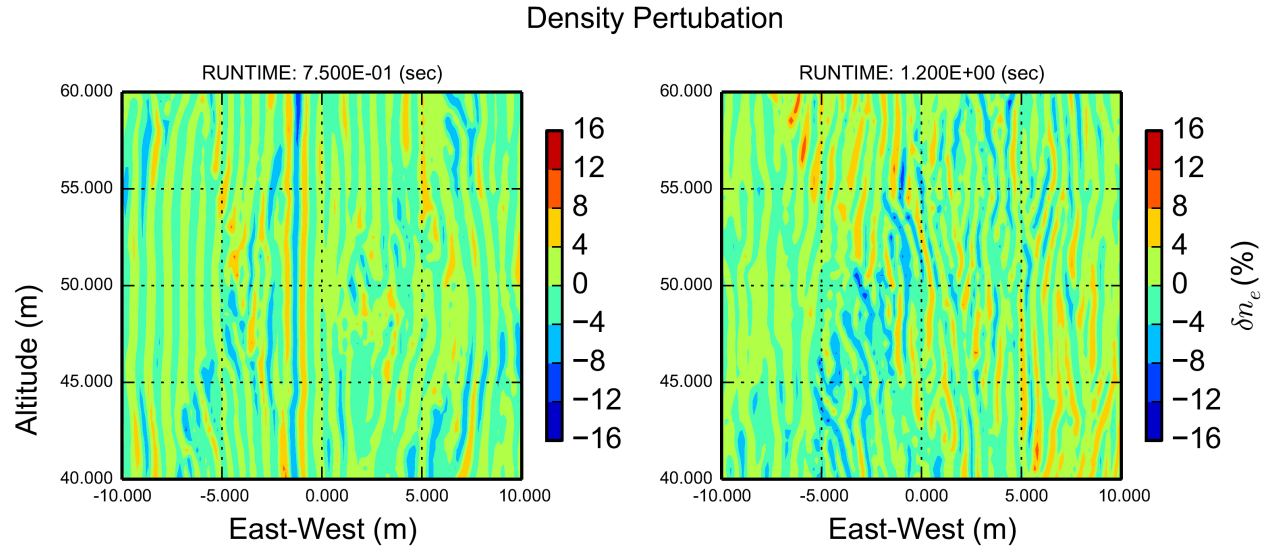


Figure 9. A close view of the large-scale structures formed during the transition phase (left-panel) and small-scale structures formed during the saturation phase of the simulation under the solar-maximum conditions.

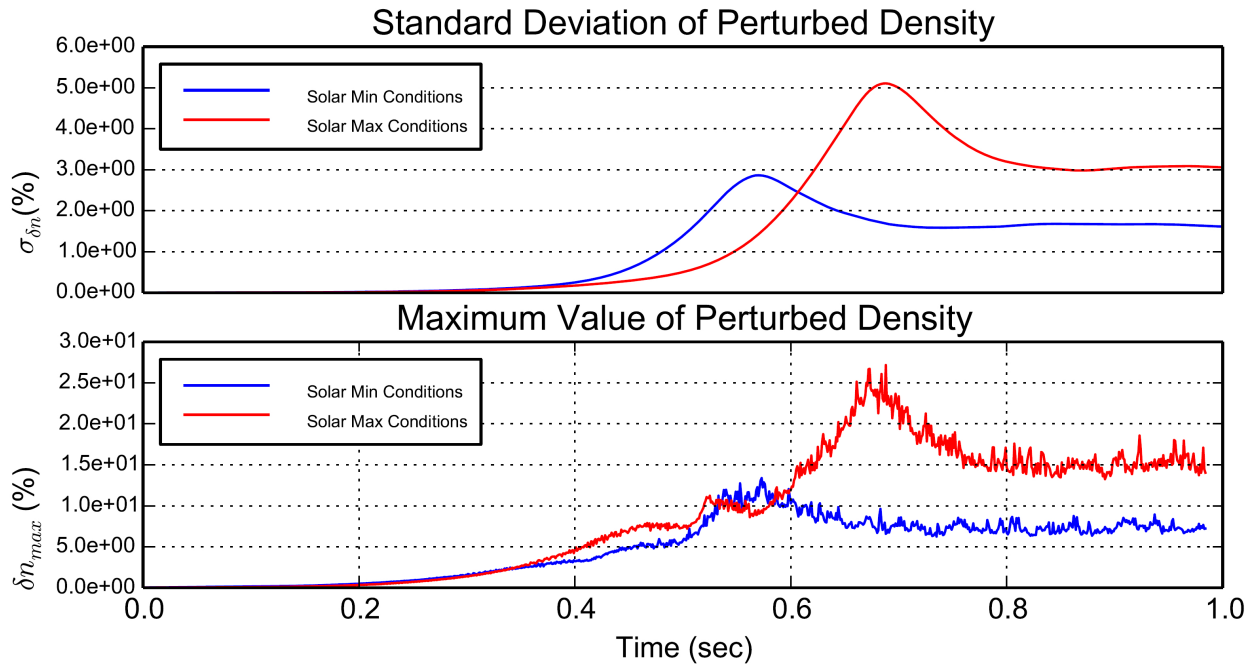


Figure 10. A comparison between the the perturbed density maxima (top panel) and its stadard deviations (bottom panel) in the solar-maximum (blue-line) and solar-minimum (red-line) conditions. The standard deviations in the lower panel also defines clearly the growing, transion, and saturation phases during the simulation under two different solar conditions.

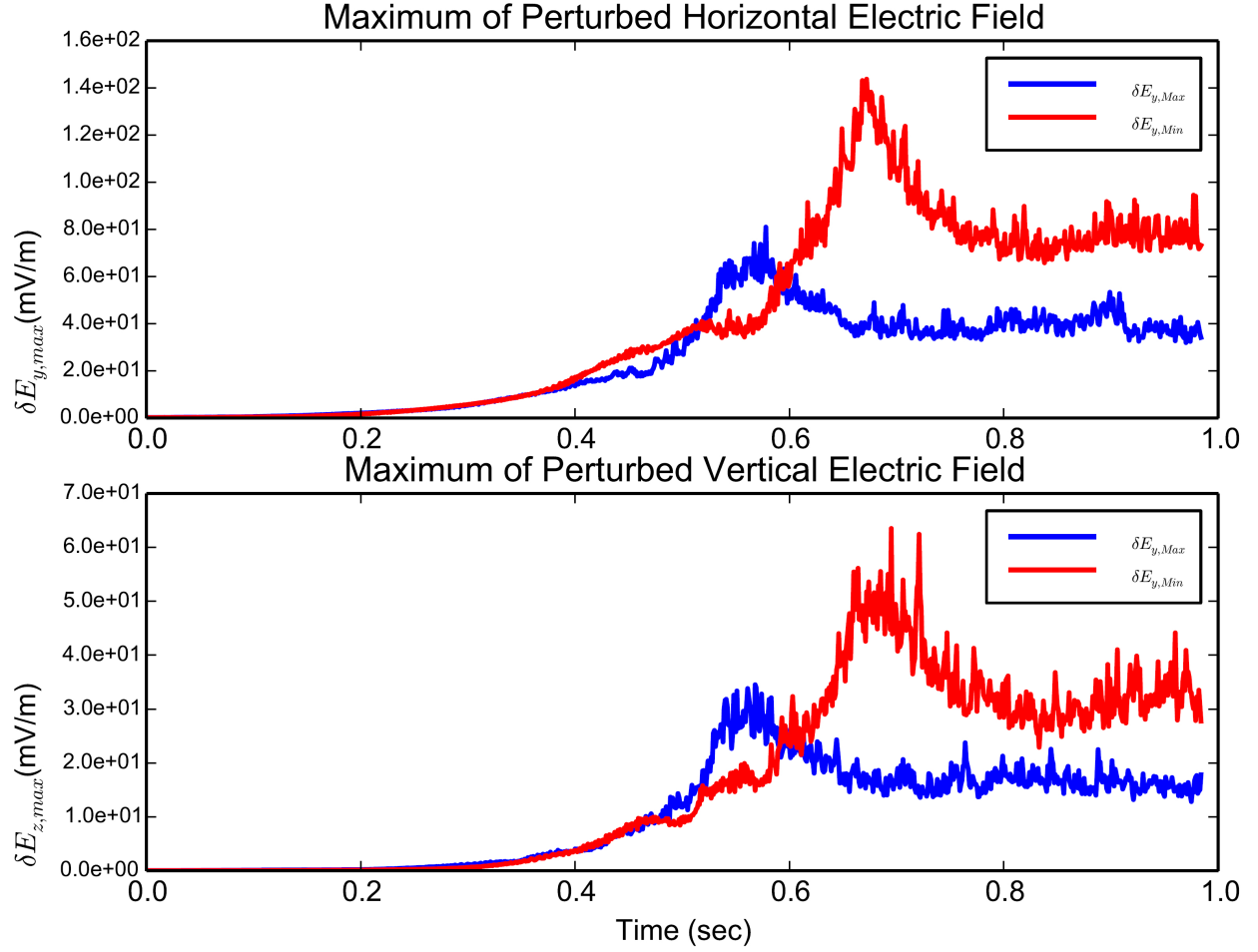


Figure 11. A comparison between the maximum perturbed electric field components in the horizontal (top panel) and vertical (bottom panel) directions in the solar-maximum (red-line) and solar-minimum (blue-line) conditions shows the effect of solar activity on the magnitude of the perturbed electric field components.

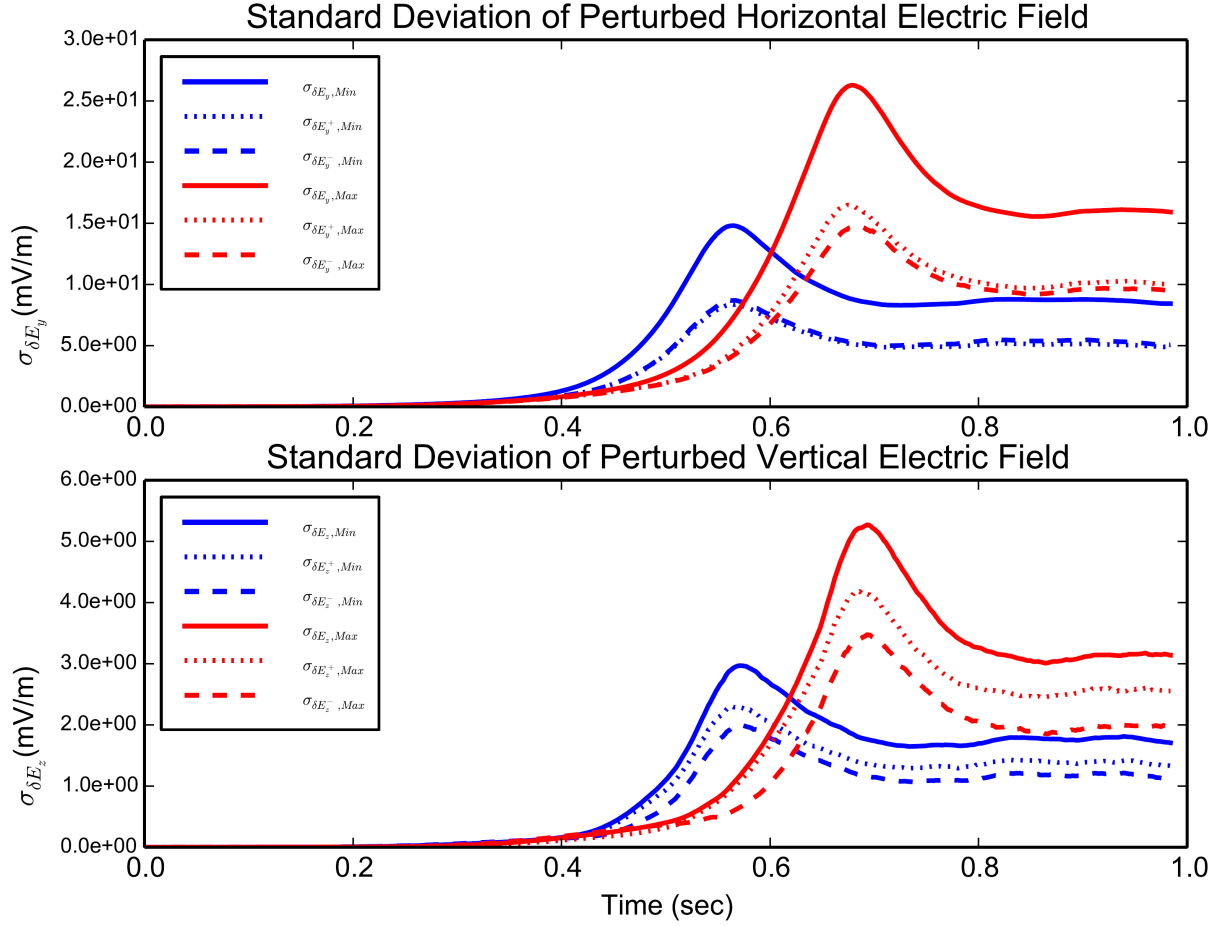


Figure 12. A comparison between the root-mean-square of the perturbed electric field components in the horizontal (top panel) and vertical (bottom panel) directions in the solar-maximum (blue-line) and solar-minimum (red-line) conditions. The dotted (dashed) lines show the root-mean-square of the positive (negative) component of the perturbed electric field.

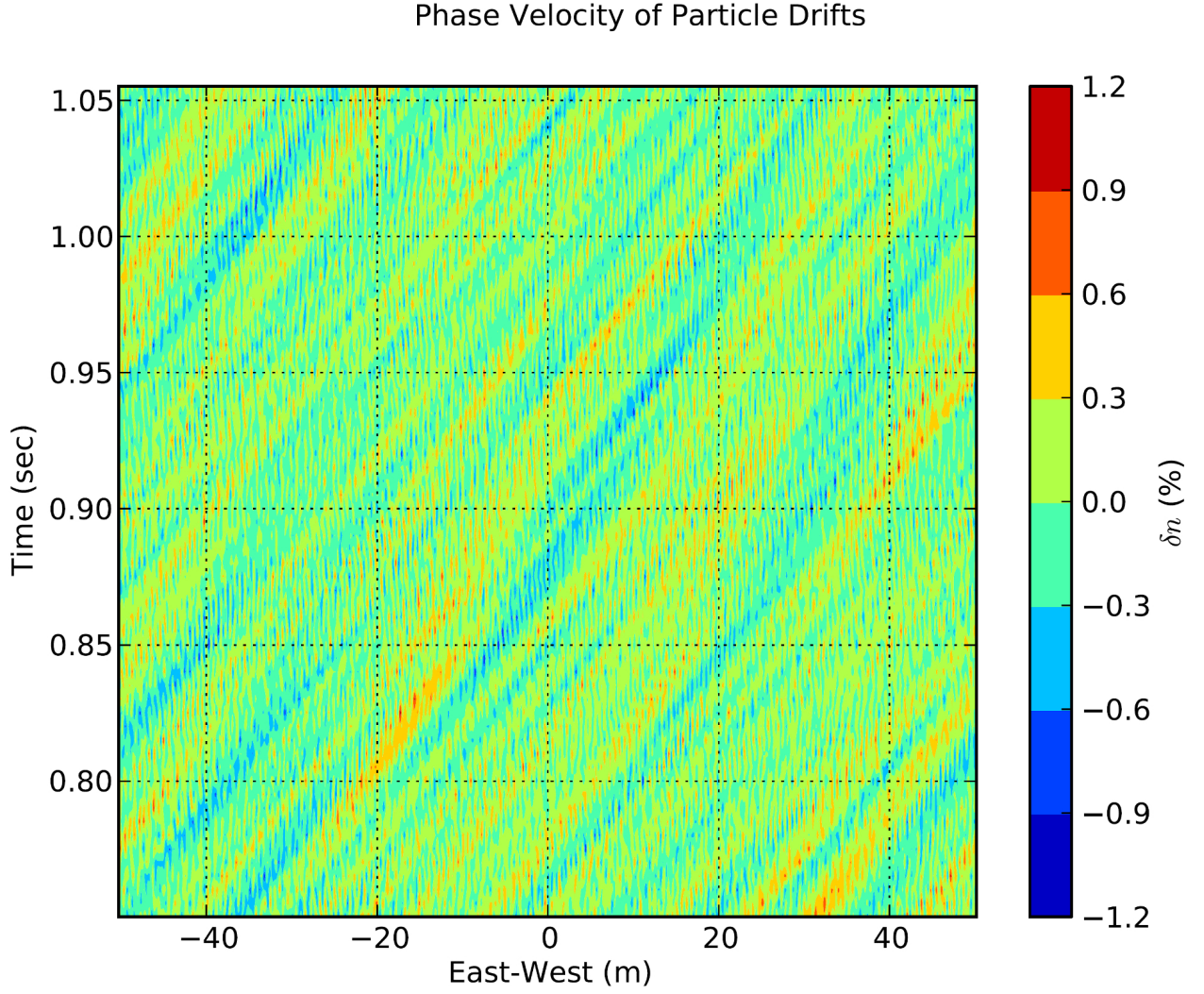


Figure 13. The inverse fourier transform of the particle density spectrum of all k_y values at $k_z=0$ (m^{-1}) for each time step during the saturation region. A phase velocity of 330 (m/s) can be estimated from the slope as the drift speed of the density to be close to the ion-acoustic speed at 105 m altitude under the solar-minimum conditions.